

UNIVERSIDAD SAN FRANCISCO DE QUITO USFQ

Colegio de Ciencias e Ingeniería

Characterization of extra-axonal
molecular diffusion of white-matter
phantoms with magnetic resonance with
artifacts correction

Patricia Estefanía Coronel Paucar

Física

Trabajo de titulación presentado como requisito

para la obtención del título de

Física

May 21, 2024

UNIVERSIDAD SAN FRANCISCO DE QUITO USFQ

Colegio de Ciencias e Ingeniería

**HOJA DE CALIFICACIÓN DE TRABAJO DE FIN DE
CARRERA**

Patricia Estefanía Coronel Paucar

Nombre del profesor, Titulo académico: Gonzalo A. Álvarez, PhD

Nombre del profesor, Titulo académico: Dario Niebieskikwiat, PhD

May 21, 2024

© Derechos de Autor

Por medio del presente documento certifico que he leído todas las Políticas y Manuales de la Universidad San Francisco de Quito USFQ, incluyendo la Política de Propiedad Intelectual USFQ, y estoy de acuerdo con su contenido, por lo que los derechos de propiedad intelectual del presente trabajo quedan sujetos a lo dispuesto en esas Políticas.

Asimismo, autorizo a la USFQ para que realice la digitalización y publicación de este trabajo en el repositorio virtual, de conformidad a lo dispuesto en la Ley Orgánica de Educación Superior del Ecuador.

Nombres y apellidos: Patricia Estefanía Coronel Paucar

Código: 00212109

Cédula de Identidad: 0105940068

Lugar y fecha: May 21, 2024

ACLARACIÓN PARA LA PUBLICACIÓN

Nota: El presente trabajo, en su totalidad o cualquiera de sus partes, no debe ser considerado como una publicación, incluso a pesar de estar disponible sin restricciones a través de un repositorio institucional. Esta declaración se alinea con las prácticas y recomendaciones presentadas por el Committee on Publication Ethics COPE descritas por Barbour et al. (2017) Discussion document on best practice for issues around theses publishing, disponible en <http://bit.ly/COPETheses>

UNPUBLISHED DOCUMENT

Note: The following capstone project is available through Universidad San Francisco de Quito USFQ institutional repository. Nonetheless, this project – in whole or in part – should not be considered a publication. This statement follows the recommendations presented by the Committee on Publication Ethics COPE described by Barbour et al. (2017) Discussion document on best practice for issues around theses publishing available on <http://bit.ly/COPETheses>

Agradecimientos

A mis padres, Ximena y Patricio, que siempre confiaron en mí, me apoyaron incondicionalmente y me dieron el privilegio de poder estudiar la carrera de mis sueños. A mi hermano Pablo, por ser mi cómplice desde que llegó al mundo a alegrarme la vida. A Lulú y Lucas, por darme el cariño más sincero. A todas mis amigas, sin ellas, no miraría el mundo de la misma manera. A todos mis amigos, especialmente a Jorge, Pablo M, Camilo, Enrique, Pablo P, Adrián, Harjit y Juanzu, por haber sido, durante cinco años, mis compañeros de clase, de vida y de risas. A Capa, por ser un amigo y maestro que quiero mucho y que me enseñó demasiado. Gracias por la paciencia. A mis profesores de la carrera, que fueron inspiración en mi vida académica, especialmente a Melissa, que siempre estuvo dispuesta a ayudarme. A Darío, por su rol como revisor de esta tesis y por proporcionarme valiosa retroalimentación. A Gonza, que me dio el privilegio de trabajar junto a él y me brindó su guía en todo este proceso. Gracias por haber sido mi maestro sin tener la obligación, lo valoraré siempre.

Finalmente, agradezco con todo mi corazón a Alejandro, con quien he estado de la mano acompañándonos y apoyándonos durante nuestras carreras universitarias.

Quien me hizo café todas las noches para estudiar, quien me dio un abrazo cada vez que quería rendirme y quien es la luz de todos mis días.

Por estas y mil razones más, gracias a todas y todos.

Un abrazo, Estefanía.

Resumen

Este estudio se centra en la caracterización de los parámetros de difusión que describen la difusión molecular en el espacio extra-axonal de los fantasmas de materia blanca utilizando secuencias de Eco de Espín con Gradiente Pulsado (PGSE) en Resonancia Magnética Nuclear (NMR), basándose en la corrección de datos debido a artifacts¹. Al calibrar con precisión el sistema de gradiente y corregir los errores relacionados con la orientación del gradiente en la secuencia PGSE, logramos mediciones de difusión fiables. Los datos obtenidos son consistentes con la literatura existente sobre los procesos de difusión.

Para caracterizar los parámetros de difusión, uno de los objetivos de este trabajo fue caracterizar la difusión del fantoma ensamblado en el laboratorio en diferentes direcciones espaciales para complementar las caracterizaciones previas realizadas en el laboratorio, que se limitaron a una sola dirección espacial. Además, este estudio contribuye a corregir datos contra artifacts inducidos por errores de calibración del hardware.

¹El término *artifacts* se refiere a errores sistemáticos en los datos de medición que pueden distorsionar los resultados de un experimento o análisis.

Se emplearon dos modelos fenomenológicos: la Ley de Potencia y el Aproximante de Padé. Los resultados revelan variaciones significativas en la tortuosidad con la orientación de la difusión, indicando que los modelos predicen una saturación a ángulos más altos, sugiriendo la máxima complejidad en las vías de difusión.

Se identificaron escalas temporales características para la transición de la difusión libre a la restringida, influenciadas por la alineación de las fibras y la complejidad estructural, alineándose con teorías previas. Estos hallazgos mejoran la precisión de la medición y el modelado de la difusión en NMR, proporcionando una comprensión más profunda de la dinámica de difusión.

Las implicaciones de estos resultados son significativas para la imagen médica, donde una comprensión precisa de los procesos de difusión es crucial. La investigación futura se centrará en aplicar ecuaciones para la longitud y el tiempo de correlación a las curvas de difusión corregidas, con el objetivo de mejorar el modelado y la predicción de los procesos de difusión. Este trabajo subraya la importancia de una caracterización precisa de la difusión para avanzar en las técnicas de diagnóstico y comprender las propiedades microestructurales de los tejidos, particularmente en el contexto de enfermedades neurodegenerativas.

Palabras clave: *Eco de Espín con Gradiente Pulsado (PGSE), Resonancia Magnética Nuclear (NMR), Difusión Molecular, Fantomas de Materia Blanca, Tortuosidad, Enfermedades Neurodegenerativas*

Abstract

This study focuses on the characterization of diffusion parameters describing molecular diffusion in the extra-axonal space of white-matter phantoms using Pulsed Gradient Spin Echo (PGSE) sequences in Nuclear Magnetic Resonance (NMR), based on data correction due to artifacts. By accurately calibrating the gradient system and correcting errors related to the gradient orientation in the PGSE sequence, we achieve reliable diffusion measurements. The obtained data are consistent with existing literature on diffusion processes.

To characterize the diffusion parameters, one of the objectives of this work was to characterize the diffusion of the phantom assembled in the laboratory in different spatial directions to complement previous characterizations conducted in the laboratory, which were limited to a single spatial direction. Additionally, this study contributes to correcting data against artifacts induced by hardware calibration errors.

Two phenomenological models are employed: the Power Law and the Padé Approximant. The results reveal significant variations in tortuosity with diffu-

sion orientation, indicating that the models predict saturation at higher angles, suggesting maximum complexity in diffusion pathways.

Characteristic timescales for the transition from free to restricted diffusion are identified, influenced by fiber alignment and structural complexity, aligning with previous theories. These findings enhance the accuracy of diffusion measurement and modeling in NMR, providing a deeper understanding of diffusion dynamics.

The implications of these results are significant for medical imaging, where a precise understanding of diffusion processes is crucial. Future research will focus on applying equations for correlation length and time to the corrected diffusion curves, aiming to improve the modeling and prediction of diffusion processes. This work underscores the importance of accurate diffusion characterization in advancing diagnostic techniques and understanding the microstructural properties of tissues, particularly in the context of neurodegenerative diseases.

Keywords: *Pulsed Gradient Spin Echo (PGSE), Nuclear Magnetic Resonance (NMR), Molecular diffusion, White-Matter Phantoms, Tortuosity, Neurodegenerative Diseases*

Contents

1	Introduction	17
2	Nuclear magnetic resonance	21
2.1	Nuclear magnetic resonance	21
2.1.1	Quantum mechanics and nuclear spin	22
2.1.2	Magnetization	24
2.1.3	Rotating frame transformation and the resonant RF field	25
2.1.4	Spin-Lattice and Spin-Spin Relaxation	31
2.2	Pulse sequences	34
2.2.1	Spin Echo	34
2.2.2	Pulse Gradient Spin Echo (PGSE)	35

	11
3 Molecular diffusion	38
3.1 Molecular Diffusion	38
3.1.1 Free Diffusion	39
3.1.2 Restricted Diffusion	41
3.1.3 Tortuosity and Effective Diffusion in Porous Media	43
4 Characterization of apparent diffusion coefficients of the extra-axonal space of the white-matter phantom	45
4.1 Measurement of diffusion coefficient using PGSE sequence	47
4.1.1 Free water, Unrestricted Diffusion as a Function of Diffusion Orientation θ	51
4.1.2 Calibrating the gradient system	52
4.2 Geometrical Analysis of Restricted Diffusion	56
4.2.1 Restricted Diffusion as a Function of Diffusion Time Δ	56
4.2.2 Restricted Diffusion as a Function of Diffusion Orientation θ	57
4.2.3 Fibers Diffusion as a Function of Diffusion Time Δ	60
5 Quantitative analysis of the hindered diffusion within the extra-	

	12
axonal space	66
5.1 Difussion Parameters	66
5.1.1 Tortuosity	66
5.1.2 Convergence times to tortuosity	69
6 Conclusions	73
Bibliography	76

List of Figures

- 2.1 Left: The decaying signal with a sinusoidal part shows the Free Induction Decay (FID), combining exponential decay due to transverse relaxation (T_2) and oscillations from Larmor precession (ω_0). Right: In the rotating frame, the FID signal is simplified to show only the exponential decay, removing the oscillatory component and highlighting the T_2 relaxation process. 28
- 2.2 The behavior of nuclear spins under a resonant RF magnetic field is described by the dynamics of a magnetization vector. In (a) the evolution within the laboratory frame is presented, characterized by the influence of a longitudinal magnetic field, B_0 , and a transverse rotating field, B_1 . At resonance, the rotation rate ω aligns with $\omega_0 = \gamma B_0$, causing the magnetization vector to precess around B_0 at ω_0 and around B_1 at ω_1 . In (b) the scenario is depicted in the rotating frame where B_1 appears stationary. At resonance in this frame, the effective longitudinal field is nullified, emphasizing the precession around B_1 . Image taken from [1]. 31

- 2.3 Left: Longitudinal relaxation (T_1) shows how the magnetization M_z gradually returns to its equilibrium value M_0 after being disturbed. The recovery follows an exponential curve modeled as equation (2.23). Right: Transverse relaxation (T_2) depicts the exponential decay of the transverse magnetization components M_x and M_y over time, modeled as equation (2.25). This decay represents the loss of phase coherence among spins. 33
- 2.4 The sequence begins with (1) the initial alignment of the magnetization vector \mathbf{M} along the external magnetic field. (2) A 90° pulse along the x -axis tips \mathbf{M} into the transverse plane. (3) Magnetization vectors then undergo free induction decay, depicted by their spread in the plane due to magnetic field inhomogeneities. (4) At τ , a 180° pulse along the x -axis is applied, flipping the vectors to the opposite side. (5) This leads to rephasing of the vectors as they converge back towards alignment. (6) Complete rephasing occurs at 2τ , forming a spin echo, with the magnetization vector again fully horizontal but opposite the initial direction. The sequence and timing of the pulses are marked on the timeline above, with red bars indicating the application of the 90° and 180° pulses. 35
- 2.5 PGSE sequence with gradient amplitude g , pulse duration δ , and gradient pulse spacing Δ . τ is the time between the 90° and 180° RF pulse. 37

3.1	Representation of a transverse cross-section of axonal tracts (gray figures) and the diffusion in the interstices. The black path indicates the movement of water in free diffusion.	39
3.2	Representation of a transverse cross-section of axonal tracts (gray figures) and the diffusion in the interstices. The red path indicates the movement of water in restricted diffusion.	41
3.3	Representation of a transverse cross-section of axonal tracts (gray figures) and the diffusion in the interstices. The green path indicates the movement of water in tortuous diffusion.	43
4.1	Transverse phantom image obtained by the NMR technique. (a) Large Fiber (restricted) ROI. (b) Small Fiber (restricted) ROI. (c) Free Water (unrestricted) ROI. Acquisition in field of view 15×15 mm with a slice thickness of 1 mm, and a resolution of 192×90 px.	48
4.2	Representation of the Normalized Magnetization signal decay of the Large and Small Fiber, respectively, at $\Delta = 8.1$ ms.	49
4.3	Normalized free water diffusion coefficient as a function of θ	51
4.4	(a) The plot illustrates the fit 4.12 applied to the corrected curves of the experimental values of the diffusion coefficient as a function of θ . (b) The fitting parameters σ and D_0 are displayed. A red horizontal line indicates the mean value of each parameter.	54

4.5	Corrected free water normalized diffusion coefficient as a function of Δ	56
4.6	(a) and (b) depict the D versus θ plots for large and small fibers, respectively. In both graphs, the curves represent the corrected apparent diffusion coefficient (D_{app}) values.	58
4.7	(a) and (b) depict the D versus θ plots for large fiber, small fiber, and free water at diffusion times $\Delta = 8.102782$ ms and $\Delta = 50.0$ ms, respectively. The blue curves represent free water, red curves represent large fibers, and green curves represent small fibers. Both experimental (Exp) and corrected (Corr) data are shown.	59
4.8	Experimental data of Large fiberfibers D/D_0 as a function of Δ fitted with the Power Law model. The scatter points represent the experimental data, while the curves represent the fitting.	63
4.9	Experimental data of fibers D/D_0 as a function of Δ fitted with the Padé Aproximant. The scatter points represent the experimental data, while the curves represent the fitting.	65
5.1	Tortuosity $1/\alpha$ as a function of θ for the Power Law and Padé Approximant models.	67
5.2	β_1 as a function of θ for the Power Law model.	69
5.3	Θ as a function of θ for the Padé Approximant model.	71

Chapter 1

Introduction

The integration of nuclear magnetic resonance (NMR) methodologies in medical imaging has revolutionized diagnostic practices, providing clinicians with detailed insights into anatomical structures and physiological processes. NMR's versatility enables multi-parametric imaging, enhancing diagnostic accuracy and prognostic capabilities [2].

NMR imaging, known as MRI, is essential in non-invasive diagnostics but faces resolution limitations, especially at micro and sub-micrometer scales crucial for clinical and research purposes. Detecting variations in axon diameter is key for identifying early signs of neurodegenerative diseases, necessitating advanced imaging techniques.

Changes in axonal diameter can indicate diseases like multiple sclerosis, Alzheimer's, and ALS. In multiple sclerosis, axonal damage and demyelination lead to changes in

axonal diameter before clinical symptoms appear [3]. In Alzheimer's, early axonal alterations can be detected before significant neuronal loss [4]. Advanced NMR techniques like Diffusion-Weighted Imaging (DWI) and Pulsed Gradient Spin Echo (PGSE) achieve higher resolution, capturing these changes [5, 1].

Visualizing axonal diameter changes precisely is crucial for early detection and patient management, enabling timely intervention and potentially slowing disease progression. Early identification of axonal damage in multiple sclerosis can prompt earlier therapy initiation, while in Alzheimer's, it can aid patient stratification for clinical trials [6]. Moreover, precise measurements enhance understanding of disease mechanisms, correlating imaging findings with clinical data to inform new therapeutic strategies.

DWI exploits water molecule diffusion properties to detect microscopic pathological changes [7], valuable for early disease stages like tumor development. PGSE improves diffusion measurement precision, enhancing NMR imaging resolution and detecting minute differences in diffusion rates [1].

Applying PGSE alongside DWI offers deeper insights into tissue microarchitecture and cellular morphology, extending NMR imaging utility beyond traditional boundaries. Integrating advanced pulse sequences into clinical NMR imaging protocols improves diagnostic accuracy and prognostic assessment, enabling earlier detection of pathological changes and transforming patient outcomes. Ongoing refinement of these methodologies overcomes conventional imaging limitations, advancing diagnostic capabilities.

The second chapter introduces fundamental NMR concepts, covering its historical development, quantum mechanical principles, nuclear spin, magnetization, and the effects of magnetic fields and RF pulses. It also explains spin-lattice relaxation (T_1), spin-spin relaxation (T_2), and pulse sequences like Spin Echo and PGSE.

The third chapter focuses on mathematical modeling of molecular diffusion, essential for NMR-based diffusion studies. It explores Fick's laws and the diffusion equation, differentiating between free and restricted diffusion, and discusses the influence of microstructural barriers, introducing concepts like tortuosity and effective diffusion in porous media.

The fourth chapter focus on the characterization of apparent diffusion coefficients of the extra-axonal space of a white-matter phantom. Details of the experimental methodologies, including NMR equipment setup, calibration, and sample preparation are described. It explains the process of acquiring and processing NMR images, highlighting the importance of precise calibration and error correction.

The fifth chapter presents a quantitative analysis of the hindered diffusion within the extra-axonal space of the phantom, analyzing the diffusion parameters extracted from the experimental data. It discusses variations in tortuosity with diffusion orientation using Power Law and Padé Approximant models, identifying characteristic timescales for the transition from free to restricted diffusion, influenced by fiber alignment and structural complexity. The chapter emphasizes the significance of geometric constraints on diffusion dynamics and provides a compre-

hensive analysis of the findings, demonstrating how advanced modeling enhances diffusion measurement accuracy and understanding.

Chapter 2

Nuclear magnetic resonance

2.1 Nuclear magnetic resonance

The beginning of NMR can be traced back to the early 20th century, with the development of quantum mechanics providing the theoretical framework necessary to understand the magnetic properties of atomic nuclei. The fundamental experiments by Isidor Rabi in the 1930s, which demonstrated the magnetic resonance of atomic beams, laid the groundwork for NMR, earning him the Nobel Prize in Physics in 1944. This was followed by the pioneering work of Felix Bloch and Edward Mills Purcell in the late 1940s, who independently discovered nuclear magnetic resonance in bulk matter, a breakthrough that would earn them the Nobel Prize in Physics in 1952 [2].

This chapter delves into the physical principles behind NMR, exploring how it

exploits the quantum behavior of atomic nuclei when exposed to magnetic fields and radiofrequency (RF) pulses. Through the lens of classical mechanics and quantum theory, we will unravel how NMR harnesses the intrinsic properties of nuclear spins to yield unparalleled insights into molecular structures, dynamics, and interactions. By dissecting the fundamental equations and concepts, this chapter aims to equip readers with a thorough understanding of NMR's theoretical foundations.

2.1.1 Quantum mechanics and nuclear spin

Nuclear Magnetic Resonance (NMR) is a manifestation of quantum mechanics at work, illustrating the unique interaction between nuclear spins and external magnetic fields. At the heart of this interaction is the quantum mechanical concept of spin (I), an intrinsic form of angular momentum carried by atomic nuclei, which is quantized according to quantum theory. This spin gives rise to a nuclear magnetic moment (μ), fundamental to the NMR phenomenon, described by the equation:

$$\mu = -\gamma\mathbf{I} \tag{2.1}$$

where γ denotes the gyromagnetic ratio, specific to each type of nucleus and \mathbf{I} is the spin angular momentum operator.

Upon application of an external magnetic field, denoted as $\mathbf{B} = B_0\hat{z}$ where B_0

is the magnetic field strength and \hat{z} is the unit vector in the direction of the field, the energy levels associated with nuclear magnetic moments split into discrete values.

The system's Hamiltonian, which describes its total energy, incorporates the interaction between the magnetic moment and the field:

$$\mathcal{H}_i = \boldsymbol{\mu}_i \cdot \mathbf{B} = -\gamma I_{i,z} B_0 \quad (2.2)$$

This shows that the energy eigenstates of nuclear spins are quantized along the magnetic field direction, resulting in distinct energy levels defined by the spin angular momentum projections, $I_{i,z} = m\hbar$, where $m = \pm\frac{1}{2}$ for nuclei with spin $\frac{1}{2}$ such as a proton (^1H).

These energy eigenstates correspond to the different orientations of spin along the field, given by the magnetic quantum number m , and are spaced by the energy difference ΔE , which the Zeeman effect captures:

$$\Delta E = \hbar\gamma B_0 \quad (2.3)$$

where \hbar is the reduced Planck constant. The condition for resonance in NMR is fulfilled when the energy of an applied radiofrequency (RF) photon equates to ΔE , prompting transitions between the spin states. These transitions yield the NMR signal, as the system absorbs or emits photons to conserve energy [8].

2.1.2 Magnetization

With the energy differential established between the two levels, the lower energy state will be predominantly occupied in accordance with the Boltzmann distribution. This uneven distribution of spin states across the energy levels culminates in a net magnetization (M) for the ensemble of nuclei, described by:

$$\mathbf{M} = \sum_i \mu_i \quad (2.4)$$

where the summation runs over all individual spins within the sample, emphasizing the collective magnetic behavior. In the presence of B_0 , nuclear spins are thermally distributed between the energy states, with a larger population residing in the ground state due to the lower energy, resulting in a net magnetization that is aligned parallel to B_0 . In NMR, the net magnetization \mathbf{M} is crucial for generating a detectable signal. For the signal to be maximized, the individual magnetic moments must align and sum up to form a sufficiently large collective magnetic moment. This coherence is essential for distinguishing between various tissues or spin types, as it affects the net magnetization's ability to interact with the applied magnetic fields and produce discernible differences in the signal.

The distribution of spin alignments and resulting magnetization is determined by the Boltzmann distribution, which at thermal equilibrium predicts a greater population in the lower energy state. The Boltzmann distribution is given by:

$$\frac{N_+}{N_-} = e^{-\Delta E/kT} \quad (2.5)$$

where N_+ and N_- are the populations of the lower and higher energy states, k is the Boltzmann constant, and T is the absolute temperature.

The dynamics of this magnetization, particularly its progression back to equilibrium after perturbation, are governed by the Bloch equations. These equations mathematically model the temporal evolution of magnetization, encapsulating the effects of relaxation processes (explained in detail in section 2.1.4).

2.1.3 Rotating frame transformation and the resonant RF field

To effectively analyze the signal of magnetization coherence in NMR, it is crucial to measure it accurately, even though perfect coherence does not last forever. Some spins precess along the magnetic field B_0 at different rates, leading to dephasing and resulting in an exponential decay of the signal, characterized by the transverse relaxation time (which will be explained in section 2.1.4). This decay describes how quickly the spins lose their coherence due to interactions and variations in the local magnetic environment.

To simplify the analysis of these precessing spins, the concept of the rotating frame is employed. This involves transforming to a reference frame that rotates at the Larmor frequency ω_0 , effectively “removing” the apparent motion of the spins

due to this precession when the rotation is about the axis of the static magnetic field. This approximation is particularly useful for protons in the same medium, such as water, because their Larmor frequencies are the same. By setting the rotating frame frequency ω to ω_0 , the effective frequency difference $\omega' = \omega - \omega_0$ becomes zero, simplifying the analysis of the decay rate.

The rotating frame transformation is mathematically represented by the unitary operator $\exp(i\omega t I_z)$, where I_z is the z -component of the angular momentum operator. The transformations for different quantum mechanical entities are:

$$\textbf{State Vector: } |\Psi'\rangle = \exp(i\omega t I_z) |\Psi\rangle \quad (2.6)$$

$$\textbf{Density Matrix: } \rho' = \exp(i\omega t I_z) \rho \exp(-i\omega t I_z) \quad (2.7)$$

$$\textbf{Observable Operators: } A' = \exp(i\omega t I_z) A \exp(-i\omega t I_z) \quad (2.8)$$

These transformations adjust the frame of reference to account for the rotational effects induced by the magnetic field, simplifying the system's dynamics by focusing on deviations from this rotational motion.

In the rotating frame, the Hamiltonian is modified to include an additional term to account for the rotation, ensuring the Schrödinger equation remains valid. The transformed Hamiltonian is:

$$\mathcal{H}' = \exp(i\omega t I_z) H \exp(-i\omega t I_z) - \omega I_z \quad (2.9)$$

For a Hamiltonian governed by the Zeeman interaction in a static magnetic field

B_0 along the z -axis, we have:

$$\mathcal{H}_{\text{Zeeman}} = -\gamma B_0 I_z \quad (2.10)$$

In the rotating frame, this Hamiltonian becomes:

$$\mathcal{H}' = -\gamma B_0 I_z - \omega I_z = -(\gamma B_0 + \omega) I_z \quad (2.11)$$

resulting in an effective magnetic field in the z -direction:

$$B'_0 = B_0 - \frac{|\omega|}{\gamma} \quad (2.12)$$

This concept is particularly useful when considering the free induction decay (FID) in NMR. FID occurs after an RF pulse is applied, and the net magnetization vector begins to precess and dephase in the transverse plane. The rotating frame helps to visualize this process by transforming the complex precessional motion into a simpler form, allowing easier analysis and measurement of the decay.

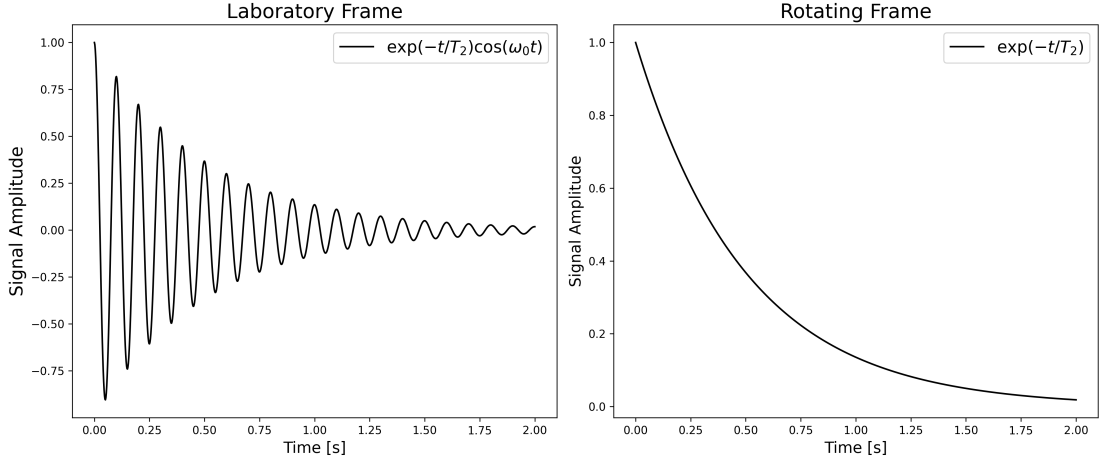


Figure 2.1: Left: The decaying signal with a sinusoidal part shows the Free Induction Decay (FID), combining exponential decay due to transverse relaxation (T_2) and oscillations from Larmor precession (ω_0). Right: In the rotating frame, the FID signal is simplified to show only the exponential decay, removing the oscillatory component and highlighting the T_2 relaxation process.

Initially, the spin system's density matrix in the laboratory frame is approximated by $\rho_{\text{lab}}(0) \approx I_z$. Transforming this to the rotating frame involves a passive rotation about the z -axis by $-\omega_0 t$, resulting in:

$$\rho_{\text{rot}}(0) = \exp(-i\omega_0 t I_z) \rho_{\text{lab}}(0) \exp(i\omega_0 t I_z) \approx I_z \quad (2.13)$$

This transformation indicates that the initial conditions remain unchanged between the laboratory and rotating frames. The active rotation induced by the RF field B_1 in the rotating frame is represented by:

$$\rho_{\text{rot}}(t) \approx \exp(i\omega_1 t I_x) I_z \exp(-i\omega_1 t I_x) \approx I_z \cos(\omega_1 t) + I_y \sin(\omega_1 t) \quad (2.14)$$

This expression shows the interconversion of spin states, with $\omega_1 = \gamma B_1$ being the

rate of this conversion. Transforming the rotating frame density matrix back to the laboratory frame requires the reverse of the initial transformation:

$$\rho_{\text{lab}}(t) \approx \exp(i\omega_0 t I_z) \rho_{\text{rot}}(t) \exp(-i\omega_0 t I_z) \quad (2.15)$$

When we introduce a resonant radiofrequency (RF) field, the Hamiltonian in the laboratory frame is:

$$\mathcal{H}_{\text{lab}} = -\gamma B_0 I_z - 2\gamma B_1 \cos(\omega t) I_x \quad (2.16)$$

This can be represented as two counter-rotating circularly polarized components. Hence, we may rewrite equation (2.16) as:

$$\mathcal{H}_{\text{lab}} = -\gamma B_0 I_z - \gamma B_1 \exp(i\omega t I_z) I_x \exp(-i\omega t I_z) - \gamma B_1 \exp(-i\omega t I_z) I_x \exp(i\omega t I_z) \quad (2.17)$$

Simplifying the transformation to the rotating frame rotating at frequency ω about the z -axis in the same (clockwise) sense as the spin phases. We find:

$$\mathcal{H}_{\text{rot}} = -\gamma \left(B_0 - \frac{\omega}{\gamma} \right) I_z - \gamma B_1 I_x - \gamma B_1 \exp(-i2\omega t I_z) I_x \exp(i2\omega t I_z) \quad (2.18)$$

At resonance ($\omega = \omega_0$), the counter-rotating component fluctuates rapidly, averaging out to zero. The effective Hamiltonian in the rotating frame simplifies to:

$$\mathcal{H}_{\text{rot}} = -\gamma \left(B_0 - \frac{\omega}{\gamma} \right) I_z - \gamma B_1 I_x \quad (2.19)$$

Here, the RF field B_1 dominates, causing the spins to nutate around the B_1 axis. This resonant condition is crucial for achieving a 90° (or $\pi/2$) pulse, which tilts the

magnetization vector into the transverse plane, representing a fundamental NMR phenomenon where equilibrium magnetization is disturbed.

The behavior of nuclear spins under a resonant RF magnetic field is described by the dynamics of a magnetization vector. In the laboratory frame, the magnetization vector precesses around B_0 at ω_0 and around B_1 at ω_1 . In the rotating frame, B_1 appears stationary, and at resonance, the effective longitudinal field is nullified, emphasizing the precession around B_1 . This results in laboratory-frame observables that exhibit both precession about the longitudinal z -axis and nutation about the transverse x -axis, reflecting the combined effects of the static and RF fields:

$$M_x = M_0 \sin(\omega_0 t) \sin(\omega_1 t), \quad M_y = M_0 \cos(\omega_0 t) \sin(\omega_1 t), \quad (2.20)$$

$$M_z = M_0 \cos(\omega_1 t) \quad (2.21)$$

where $M_0 = N\gamma\text{Tr}(I_z\rho_0)$. This combination of precession about the laboratory-frame z -axis and nutation about the rotating frame x -axis is shown in Figure 2.2.

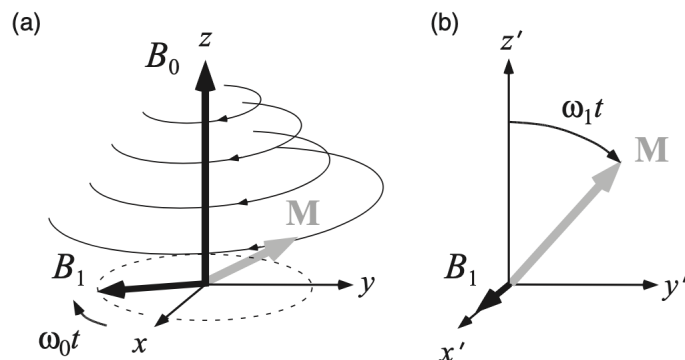


Figure 2.2: The behavior of nuclear spins under a resonant RF magnetic field is described by the dynamics of a magnetization vector. In (a) the evolution within the laboratory frame is presented, characterized by the influence of a longitudinal magnetic field, B_0 , and a transverse rotating field, B_1 . At resonance, the rotation rate ω aligns with $\omega_0 = \gamma B_0$, causing the magnetization vector to precess around B_0 at ω_0 and around B_1 at ω_1 . In (b) the scenario is depicted in the rotating frame where B_1 appears stationary. At resonance in this frame, the effective longitudinal field is nullified, emphasizing the precession around B_1 . Image taken from [1].

If the RF field is not precisely on resonance, an additional longitudinal component ($B_0 - \omega/\gamma$) appears, leading to oblique precession patterns. The effectiveness of an RF pulse is maximized when its frequency closely matches the Larmor frequency of the spins, ensuring that the RF field vector B_1 dominates the spin dynamics, allowing selective perturbations of the spin system. Detailed calculations can be found by Callaghan in [1].

2.1.4 Spin-Lattice and Spin-Spin Relaxation

Spin-lattice relaxation (T_1) describes the process by which the component of the magnetization vector along the direction of the static magnetic field B_0 returns to

its equilibrium state after being disturbed. This mechanism is fundamentally associated with the exchange of energy between the spin system and its surrounding environment, or ‘lattice’. The rate of this energy exchange is characterized by the relaxation time T_1 .

The rate of change of the longitudinal magnetization M_z is described by the differential equation:

$$\frac{dM_z}{dt} = -\frac{M_z - M_0}{T_1} \quad (2.22)$$

where M_0 is the equilibrium magnetization along B_0 . The solution to this equation gives the evolution of M_z over time:

$$M_z(t) = M_0(1 - e^{-t/T_1}) \quad (2.23)$$

This equation illustrates that $M_z(t)$ gradually returns to its equilibrium value M_0 . T_1 relaxation is influenced by the molecular environment surrounding the spins.

Spin-spin relaxation (T_2), unlike spin-lattice relaxation, involves the loss of phase coherence among spins in the transverse plane, perpendicular to B_0 . This dephasing is not directly caused by energy exchange with the lattice but rather by interactions among the spins themselves.

The rate of change of the transverse magnetization components M_x and M_y is described by:

$$\frac{dM_{x,y}}{dt} = -\frac{M_{x,y}}{T_2} \quad (2.24)$$

The solution to this equation, which describes the exponential decay of the trans-

verse magnetization, is:

$$M_{x,y}(t) = M_{x,y}(0)e^{-t/T_2} \quad (2.25)$$

This expression indicates that $M_{x,y}(t)$ decays exponentially with the characteristic time constant T_2 . Transverse relaxation T_2 is generally shorter than T_1 because it is sensitive to any interaction that causes phase shifts among spins.

These relaxation processes are critical in understanding Free Induction Decay (FID). After an RF pulse is applied, the net magnetization vector precesses and dephases in the transverse plane, producing the FID signal. The T_2 relaxation time directly affects the decay rate of the FID signal, while T_1 governs the recovery of the longitudinal magnetization, which is crucial for the signal intensity.

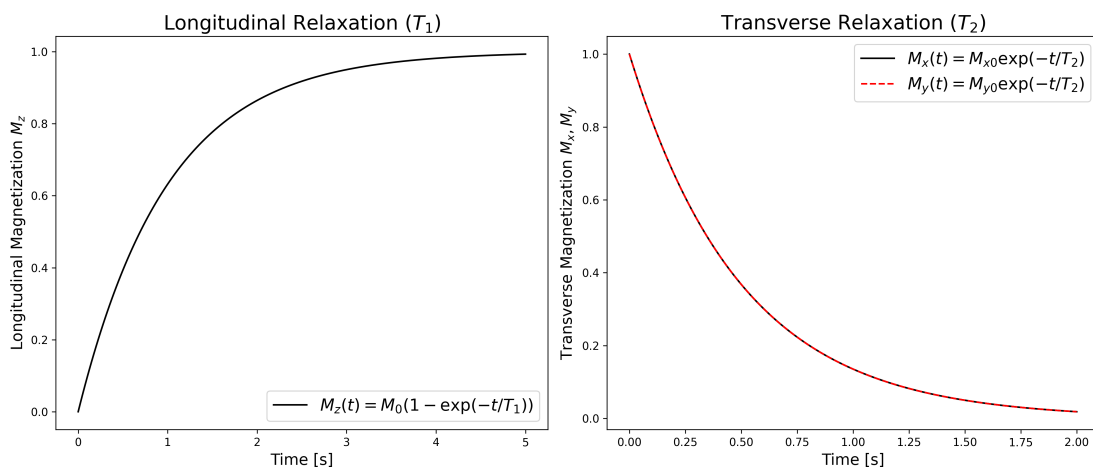


Figure 2.3: Left: Longitudinal relaxation (T_1) shows how the magnetization M_z gradually returns to its equilibrium value M_0 after being disturbed. The recovery follows an exponential curve modeled as equation (2.23). Right: Transverse relaxation (T_2) depicts the exponential decay of the transverse magnetization components M_x and M_y over time, modeled as equation (2.25). This decay represents the loss of phase coherence among spins.

2.2 Pulse sequences

2.2.1 Spin Echo

Spin echo is a phenomenon central to NMR that counteracts signal decay due to inhomogeneities in the external magnetic field. The concept was first introduced by Erwin Hahn in 1950 and has since become a fundamental technique in NMR and MRI to refocus spin magnetization, enhancing signal clarity and measurement accuracy. In an NMR experiment, the initial phase coherence of the nuclear spins is disrupted over time, predominantly due to microscopic variations in the magnetic field, resulting in signal dephasing. The spin echo sequence ingeniously reverses this dephasing through the application of a 180° RF pulse, which effectively inverts the spin system and allows the spins to rephase, forming an echo of the original NMR signal.

The Hahn echo consists of steps described in the Figure 2.4.

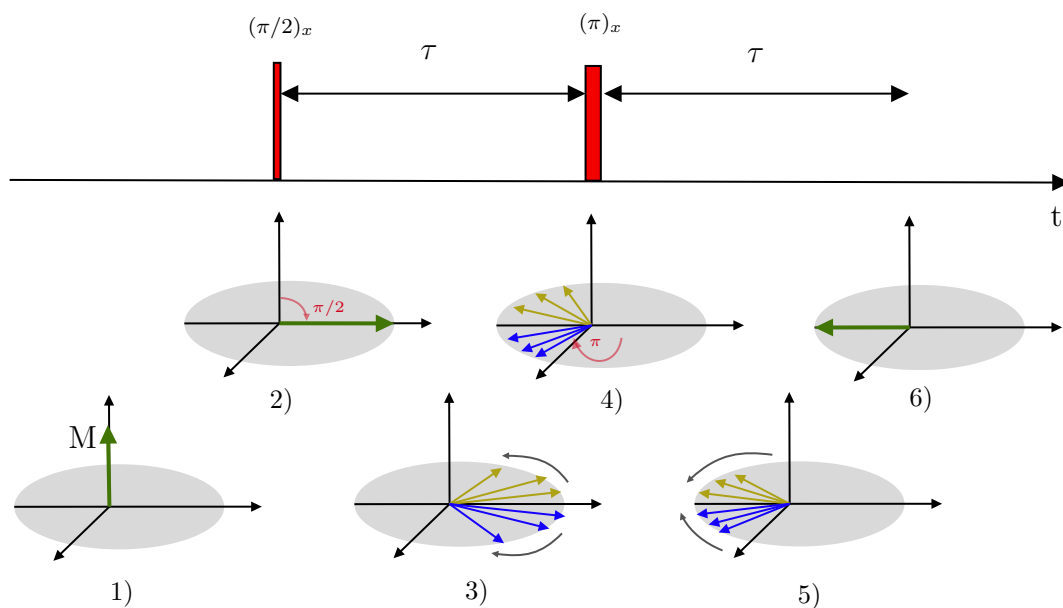


Figure 2.4: The sequence begins with (1) the initial alignment of the magnetization vector \mathbf{M} along the external magnetic field. (2) A 90° pulse along the x -axis tips \mathbf{M} into the transverse plane. (3) Magnetization vectors then undergo free induction decay, depicted by their spread in the plane due to magnetic field inhomogeneities. (4) At τ , a 180° pulse along the x -axis is applied, flipping the vectors to the opposite side. (5) This leads to rephasing of the vectors as they converge back towards alignment. (6) Complete rephasing occurs at 2τ , forming a spin echo, with the magnetization vector again fully horizontal but opposite the initial direction. The sequence and timing of the pulses are marked on the timeline above, with red bars indicating the application of the 90° and 180° pulses.

2.2.2 Pulse Gradient Spin Echo (PGSE)

The PGSE sequence is designed to measure molecular diffusion by applying magnetic field gradients, encoding and then decoding the position of spins. When spins diffuse within a medium, their positions differ at the end of the experiment. Consequently, the final gradient does not fully reverse the phase accumulated during the initial gradient, leading to a reduction in the final magnetization. Thereby,

the echo amplitude E is attenuated by diffusion, described by the Stejskal-Tanner equation:

$$E = E(0) \exp(-\gamma^2 g^2 \delta^2 t_d D) \quad (2.26)$$

where $E(0)$ is the initial echo amplitude, γ the gyromagnetic ratio, g the gradient strength, δ the duration of the gradient pulse, Δ the diffusion time, D the diffusion coefficient and $t_d = (\Delta - \delta/3)$ that is a modified diffusion time that accounts for the effective observation period of molecular diffusion in the presence of gradient pulses. This sequence allows for the investigation of microstructural environments by observing how diffusion is affected by obstacles like cell membranes [9].

Considering the equation (2.26) we can call b_{value} to the term that accompanies the diffusion coefficient and define it as $b_{\text{value}}(\Delta, \delta) = \gamma^2 g^2 \delta^2 t_d$.

The PGSE sequence is pivotal for measuring diffusion in MRI. It involves the application of two gradient pulses separated by a 180° RF pulse, as shown in Figure 2.5. The first gradient pulse dephases the spins, while the 180° pulse inverts their phase, allowing the second gradient pulse to rephase them, forming a spin echo. The attenuation of the echo amplitude by diffusion is quantified by the Stejskal-Tanner equation, providing insights into the microstructure of the tissue.

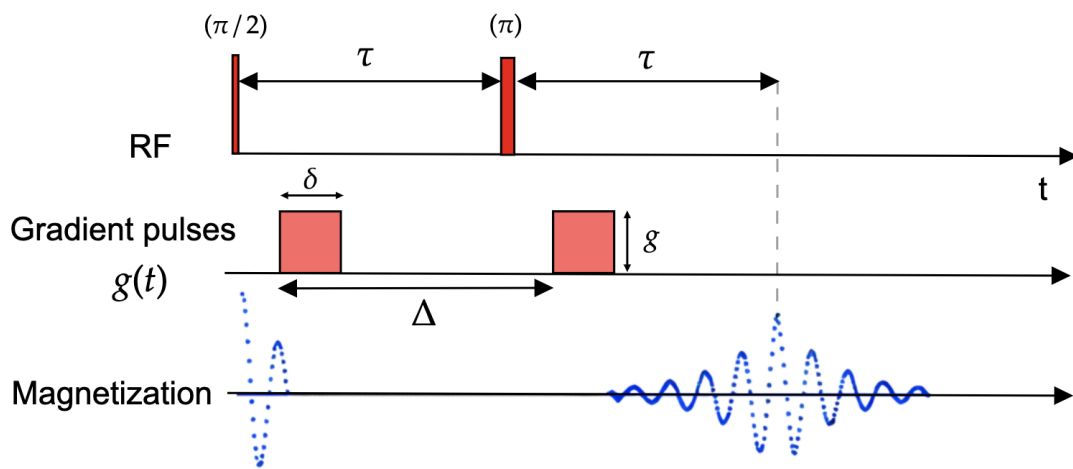


Figure 2.5: PGSE sequence with gradient amplitude g , pulse duration δ , and gradient pulse spacing Δ . τ is the time between the 90° and 180° RF pulse.

Chapter 3

Molecular diffusion

3.1 Molecular Diffusion

Diffusion is a fundamental process describing the movement of particles from regions of higher concentration to lower concentration. The molecular diffusion process can be described by Fick's laws, where the first law,

$$J = -D\nabla\phi \tag{3.1}$$

relates the diffusion flux J to the diffusion coefficient D and the concentration gradient $\nabla\phi$.

This chapter delves into the physical principles of diffusion, guided by insights from NMR studies, to unravel the intricacies of molecular motion. Through NMR,

we gain a unique lens to observe diffusion, enabling the quantification and visualization of this essential process in real-time and in situ [1].

3.1.1 Free Diffusion

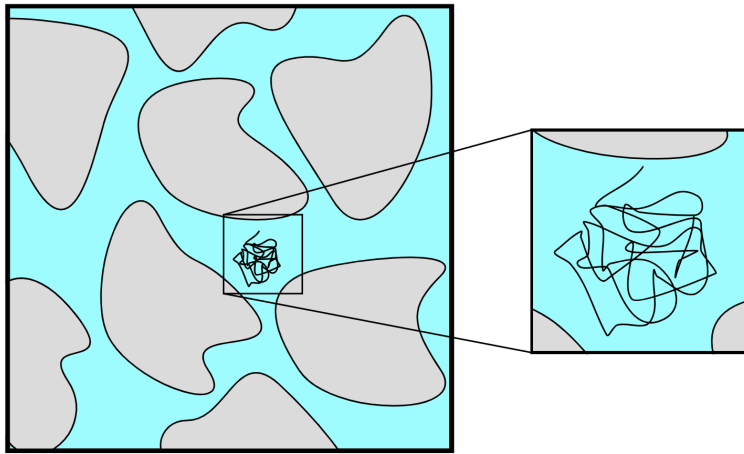


Figure 3.1: Representation of a transverse cross-section of axonal tracts (gray figures) and the diffusion in the interstices. The black path indicates the movement of water in free diffusion.

In an ideal scenario where spins are free to move, the motion can be modeled as a random walk. This random motion in three-dimensional space can be described mathematically considering that the displacements are uncoupled and the motions in any direction are equiprobable. The following equation describes the motion in one dimension for each discrete site i on a lattice with a grid of separation l :

$$W_i(t + \Delta t) = \frac{1}{2}W_{i-1}(t) + \frac{1}{2}W_{i+1}(t) \quad (3.2)$$

where $W_i(t)$ represents the probability of finding a nucleus at site i at time t .

Transitioning to a continuum by applying a Taylor expansion, we derive the diffusion equation:

$$\frac{\partial W}{\partial t} = D_0 \frac{\partial^2 W}{\partial x^2} \quad (3.3)$$

where D_0 represents the diffusion coefficient, characterized by [10]:

$$D_0 = \lim_{\Delta t \rightarrow 0, l \rightarrow 0} \frac{l^2}{2\Delta t} \quad (3.4)$$

This diffusion coefficient is fundamental in describing how the macroscopic diffusion process emerges from microscopic random walks, historically derived by Albert Einstein for Brownian motion. The mean square displacement, in one dimension, is given by:

$$\langle (x(t) - x(0))^2 \rangle = 2D_0 t \quad (3.5)$$

and, in three dimensions,

$$\langle (\mathbf{r}(t) - \mathbf{r}(0))^2 \rangle = 6D_0 t \quad (3.6)$$

3.1.2 Restricted Diffusion

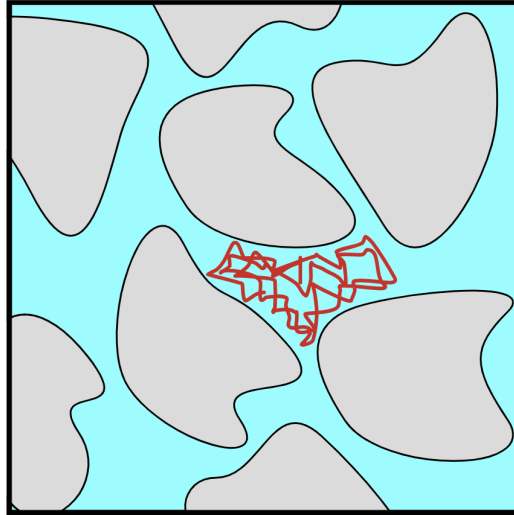


Figure 3.2: Representation of a transverse cross-section of axonal tracts (gray figures) and the diffusion in the interstices. The red path indicates the movement of water in restricted diffusion.

In biological tissues, diffusion is often restricted by cellular structures, altering the free diffusion model. The mean square displacement no longer follows the linear relationship and is described by equation (3.1.2) that describes short times. For longer times, where diffusion encounters physical barriers, the displacement saturates due to these restrictions, indicating the physical limits imposed by the microstructure.

The saturation level can be related to the microstructural geometry, necessitating the treatment of $x(t)$ as a stochastic variable. Analyzing a stochastic variable involves defining its behavior through its autocorrelation function $\langle x(t)x(0) \rangle$, which measures the ‘memory’ of the process by indicating how correlated a variable remains with its past states. At $t = 0$, the autocorrelation function equals the mean

squared value of the variable $\langle x^2 \rangle$.

As time progresses, the autocorrelation typically decays, reflecting the diminishing influence of the initial state on $x(t)$. The decay rate of this function is crucial for understanding how quickly the properties of the system change over time. The autocorrelation function can be normalized to yield the autocorrelation decay function $g(t)$, expressed as

$$g(t) = \frac{\langle x(t)x(0) \rangle - \langle x \rangle^2}{\langle x^2 \rangle - \langle x \rangle^2} \quad (3.7)$$

Here, $\langle x \rangle$ is the mean value of x . This normalization helps in comparing the correlation functions of different systems or different states of the same system on a similar scale.

The correlation time, τ_c , is a measure of the average time over which the function $g(t)$ retains significant values. It is defined as:

$$\tau_c = \int_0^{\infty} g(t) dt \quad (3.8)$$

The correlation time, τ_c measures the average duration over which $g(t)$ retains significant values, providing insights into the lasting impact of past states on future states of the system. In the context of magnetic resonance, τ_c helps describe how quickly spins lose memory of their initial orientations due to interactions with their environment.

For restricted diffusion, as $t \rightarrow \infty$, the mean square displacement equation

stabilizes:

$$\lim_{t \rightarrow \infty} \langle \Delta x^2(t) \rangle = 2D_0\tau_c = l_c^2 \quad (3.9)$$

where l_c is defined as the correlation length of the system [10].

3.1.3 Tortuosity and Effective Diffusion in Porous Media

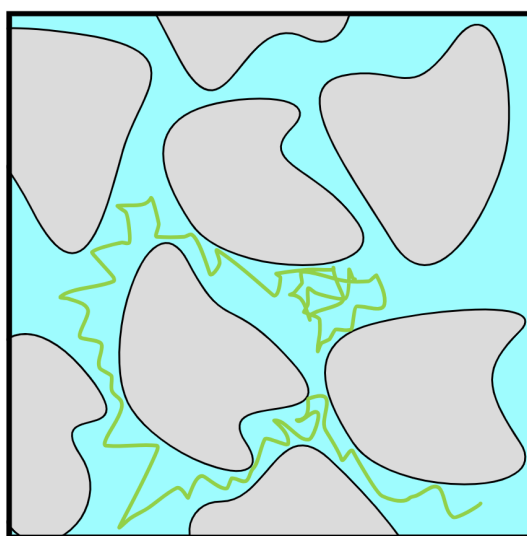


Figure 3.3: Representation of a transverse cross-section of axonal tracts (gray figures) and the diffusion in the interstices. The green path indicates the movement of water in tortuous diffusion.

Tortuosity is a key concept in the study of diffusion through porous media, which often contains regions inaccessible to diffusing particles, thereby affecting the pathway and efficiency of diffusion. The effective diffusion coefficient, $D_{\text{eff}}(t)$, captures these dynamics and is mathematically described as:

$$D_{\text{eff}}(t) = \frac{\langle (\mathbf{r}(t) - \mathbf{r}(0))^2 \rangle}{6t} \quad (3.10)$$

This expression, which is analogous to the time-dependent diffusion coefficient (3.6), quantifies the incoherent random motion of spins within the pore spaces. Over time, as more spins encounter barriers, $D_{\text{eff}}(t)$ evolves, eventually approaching a steady state that reflects the connectivity and structural complexity of the medium.

For media with well-defined correlation lengths, l_c , described in equation (3.9), the long-term behavior of diffusion is governed by the relationship:

$$\lim_{t \rightarrow \infty} \frac{D_{\text{eff}}(t)}{D_0} = \frac{D_{\text{eff}}(\infty)}{D_0} = \frac{1}{\alpha} \quad (3.11)$$

Here, $1/\alpha$ quantifies the tortuosity of the pore space, indicating how the geometric constraints of the medium impede the free diffusion of particles.

Generally, for porous media, this regime is characterized by the fact that $D_{\text{eff}}(t)$ becomes constant when $t \rightarrow \infty$. In this context, tortuosity α is defined as a measure of the connectivity between the pores in which diffusion occurs [1]. Specifically, α can provide insights into the structural complexity and the extent of the restrictions within the medium.

Chapter 4

Characterization of apparent diffusion coefficients of the extra-axonal space of the white-matter phantom

The experiment was conducted at the Spectroscopy and Nuclear Magnetic Resonance Imaging Laboratory within the Department of Medical Physics at Instituto Balseiro in Bariloche, Argentina. It was employed a 9.4 Tesla Bruker Avance III HD WB NMR spectrometer, featuring a ^1H resonance frequency of $\omega_z = 400.15$ MHz. Utilization included a *Micro 2.5* probe, which is capable of generating magnetic field gradients up to 1500 mT/m across three spatial dimensions, and equipped with a resonator diameter of 20 mm. The temperature during

the experiments was maintained at 25 °C. The objective of these measurements is to investigate the variation of the diffusion coefficient as a function of the system's evolution time. This analysis facilitates the identification of distinct diffusion regimes described in Section 3.

In this research, the experimental setup detailed in the master thesis project “Filtros Selectivos de Dinámicas Traslacionales en Microestructuras de Materia Blanca con MRI” by Lic. Ezequiel L. Saidman, supervised by Dr. Gonzalo A. Álvarez [10]. Comprehensive specifications and procedural nuances of the original experimental design are fully described in this reference.

The core objective of our replication was to observe restricted diffusion effects similar to those found in the extra-axonal regions of the brain. To this end, aramid (Kevlar) fibers with diameters approximating those of axonal structures in human and murine brains (approximately 10 μm) were used. These fibers were arranged into compact mesh-like bundles within a 15 ml Falcon tube, simulating the structured complexity of brain tissue. The assembly was immersed in distilled water to facilitate diffusion studies, mirroring the hydration conditions in neural environments. This setup is expected to exhibit three diffusive behaviors based on the interaction of water molecules with the microstructured environment.

4.1 Measurement of diffusion coefficient using PGSE sequence

In the conducted experiment, the objective was to capture images by varying the angle of gradient application from 0° (transverse) to 90° (longitudinal). Utilizing the principles of the PGSE sequence, as elucidated in Figure 2.5, the apparatus was configured to systematically alter the angle corresponding to a specified diffusion time, Δ . For this experiment, Δ was set within the range from 8.1 to 100 ms, and the b_{value} varies from 300 to $3000 \text{ s}\cdot\text{mm}^{-2}$. The experimental setup was arranged in two configurations: the first configuration captured 10 images for each angle across the specified Δ , culminating in a total of 110 images; the second configuration captured 2 images for each angle and each Δ , resulting in a total of 22 images. Additionally, the pulse duration δ was set to 2.5 ms.

For data processing, Python was employed and `brukerapi` library was used to read the data. The extraction of image information involved considering three sets of coordinates corresponding to the regions of interest (ROI) whose evolution was to be evaluated in terms of direction and pulse spacing. Figure 4.1b illustrates each ROI, distinguishing them by color: Large Fiber (red), Small Fiber (green), and Free Water (blue).

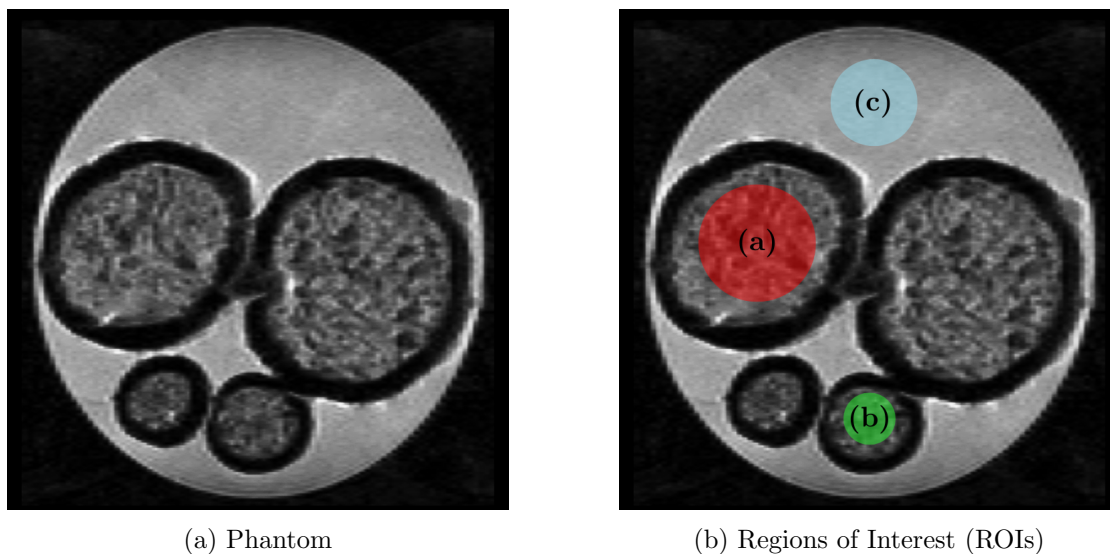


Figure 4.1: Transverse phantom image obtained by the NMR technique. (a) Large Fiber (restricted) ROI. (b) Small Fiber (restricted) ROI. (c) Free Water (unrestricted) ROI. Acquisition in field of view 15×15 mm with a slice thickness of 1 mm, and a resolution of 192×90 px.

The image data are stored in a tensor, representing spatial variations in the net magnetization of the ensemble of spins. Each pixel in the image is encoded on a grayscale spectrum, where the intensity of each pixel corresponds to the magnetization properties of the tissue being imaged. Specifically, pixels that appear white indicate tissues with very short T_1 relaxation times or very long T_2 relaxation times. Conversely, pixels that appear black correspond to regions where T_2 relaxation occurs very rapidly, indicating minimal transverse magnetization at the time of measurement. This encoding scheme allows for detailed visualization of tissue characteristics based on their magnetic relaxation properties.

Utilizing the images obtained from the spectrometer, the subsequent step involved analyzing the behavior of magnetization as a function of the b_{value} . Figure

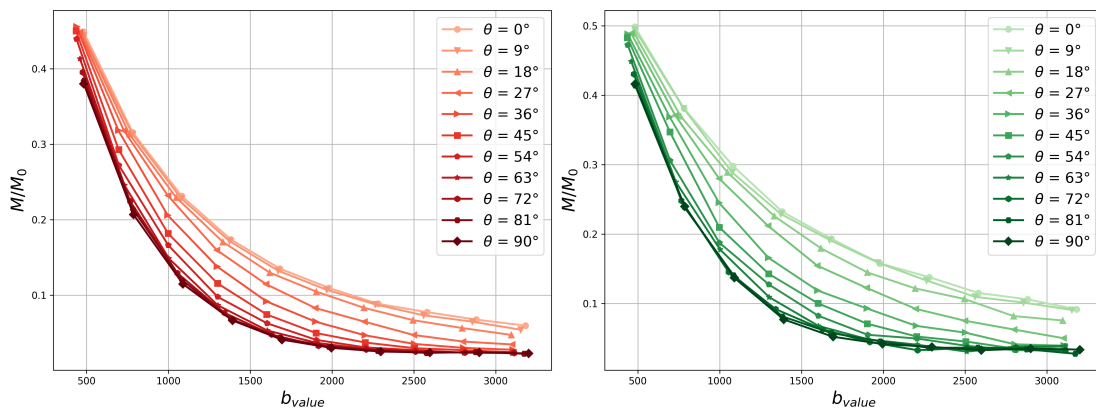


Figure 4.2: Representation of the Normalized Magnetization signal decay of the Large and Small Fiber, respectively, at $\Delta = 8.1$ ms.

4.2 illustrates the behavior of the normalized magnetization, highlighting that an increase in the b_{value} correlates with a progressive loss of signal, which may be attributable to artifacts. Additionally, as increasing the angle θ for each fiber, the signal loss signal faster.

To address the issue of signal loss, a linear fit represented as $y = ax + b$ was applied. Large b_{values} were discarded, and a range of 300 to 600 $\text{s}\cdot\text{mm}^{-2}$ was used for the fitting. This relationship was integrated with the Stejskal-Tanner equation (2.26), expressed as:

$$\ln\left(\frac{M}{M_0}\right) = -b_{\text{value}}D \quad (4.1)$$

where the diffusion coefficient value a and the intercept b were determined.

At zero gradient, the b_{value} is effectively nullified, yielding a recalibrated value for M_0 , which is crucial for normalization. Subsequently, the value b for the linear fit is used to determine the initial value. To correct further errors, it was considered that the normalization might be inaccurately applied, indicating that the

experimental form of the equation (2.26) should include a factor A to account for artifacts, as follows:

$$\frac{M}{M_0} = Ae^{-b_{\text{value}}D} \quad (4.2)$$

Thus,

$$\ln\left(\frac{M}{M_0}\right) = \ln(A) - b_{\text{value}}D \quad (4.3)$$

where $\ln(A)$ corresponds to the intercept b of the previous linear fit.

By analyzing the initial magnetization and the average diffusion coefficient for each Δ time, a constant behavior is observed only for small Δ values (up to 50 ms). Therefore, the entire calibration will be conducted using eight b_{values} , ranging from 8.1 to 50 ms.

With this adjusted normalization approach, the diffusion coefficient values were accurately determined and corrected. The initial step involves analyzing the region of interest (ROI) for free water to observe unrestricted behavior. This analysis helps determine the unrestricted diffusion coefficient, which is essential for correctly normalizing the fiber data. Furthermore, this approach facilitates a deeper investigation of the physical concepts underlying diffusion in the absence of obstacles.

4.1.1 Free water, Unrestricted Diffusion as a Function of Diffusion Orientation θ

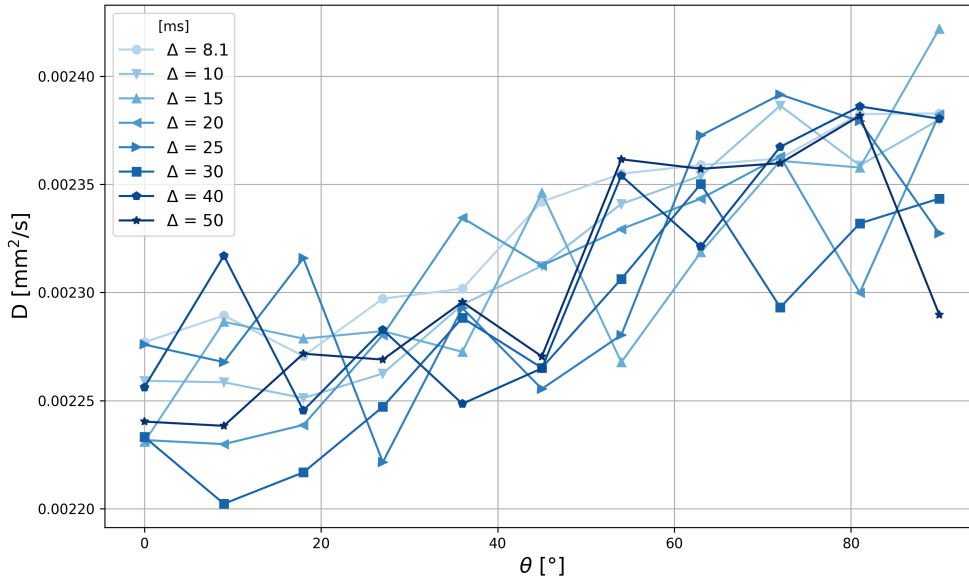


Figure 4.3: Normalized free water diffusion coefficient as a function of θ .

By plotting the water diffusion coefficient as a function of the gradient orientation, it is observed that the curves exhibit an increase, displaying behavior that is theoretically incorrect. For free water, the diffusion coefficient should remain constant regardless of the gradient angle, as there are no obstacles that might cause restricted diffusion behavior, whether the gradient is longitudinal or transverse. This indicates that there is likely a calibration error in the gradient that is affecting the results, assuming that γ and δ of the b_{value} contain no error, as the sequence remains consistent across all experiments.

4.1.2 Calibrating the gradient system

In NMR experiments, the gradient system is used to apply spatially varying magnetic fields, which are crucial for encoding spatial information and for diffusion measurements using techniques like PGSE. Ideally, these gradients should be uniform and well-calibrated to ensure accurate measurements.

However, as explained before, it is observed that the gradient strength can vary with the orientation of the applied gradient. This orientation dependency can be expressed in terms of an angle θ , which represents the direction of the gradient relative to a reference axis.

To describe the gradient vector \mathbf{g} as a function of this angle, we consider its components along the x -axis and z -axis:

$$\mathbf{g} = g_x \cos \theta \hat{x} + g_z \sin \theta \hat{z} \quad (4.4)$$

However, a discrepancy is observed between the gradient components along the x -axis and z -axis. The reference value of g_x is used as the correct one. Thus, introducing a correction Δg for g_z ,

$$g_z = g_x + \Delta g \quad (4.5)$$

Consequently, at $\theta = 0^\circ$, only the x -component is present, and at $\theta = 90^\circ$, only the z -component is dominant. This directional dependency of the gradient must be

carefully calibrated to ensure accurate measurements across different orientations.

The magnitude of the gradient vector can be calculated as follows:

$$g = |\mathbf{g}| = (g_x^2 \cos^2 \theta + g_z^2 \sin^2 \theta)^{1/2} \quad (4.6)$$

$$= (g_x^2 \cos^2 \theta + (g_x + \Delta g)^2 \sin^2 \theta)^{1/2} \quad (4.7)$$

$$= (g_x^2 + 2g_x \Delta g \sin^2 \theta + (\Delta g)^2 \sin^4 \theta)^{1/2} \quad (4.8)$$

Assuming $(\Delta g)^2 \approx 0$

$$g = g_x \left(1 + \frac{2\Delta g}{g_x} \sin^2 \theta \right)^{1/2} \quad (4.9)$$

By re-writing the equation with $\sigma = 2\Delta g/g_x$, the following expression is obtained:

$$g^2 = g_x^2 (1 + \sigma \sin^2 \theta) \quad (4.10)$$

The parameter σ contains information about the gradient g_x and the gradient error Δg . Now, replacing the gradient g into equation (2.26), this can be expressed as:

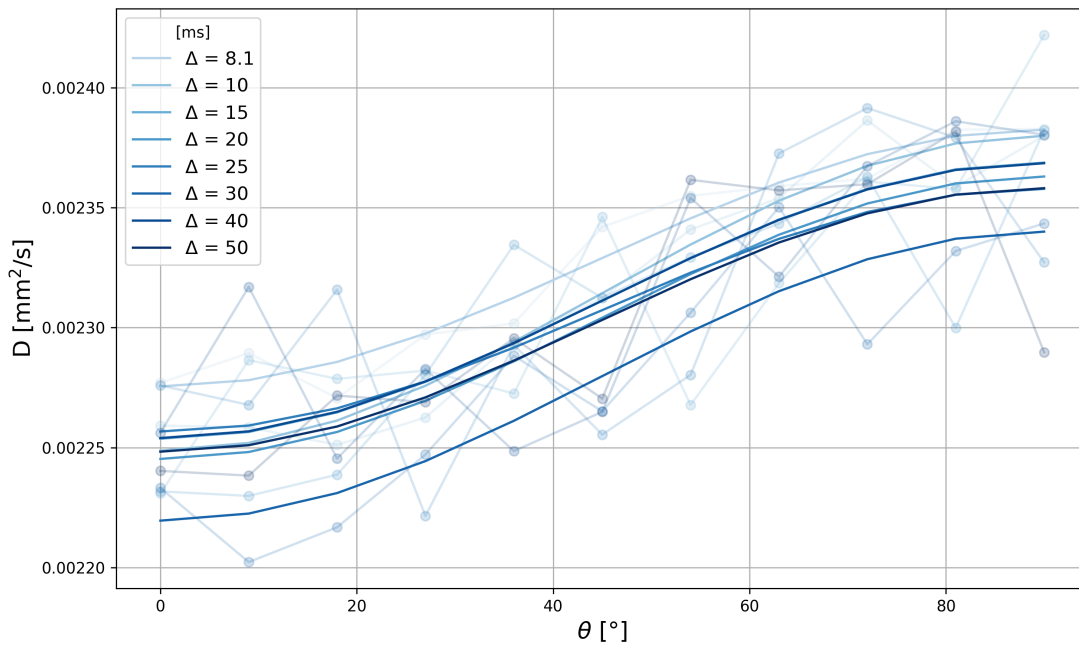
$$\ln \left(\frac{M}{M_0} \right) = -\gamma^2 \delta^2 t_d g_x^2 (1 + \sigma \sin^2 \theta) D_0 = -\gamma^2 g_x^2 \delta^2 t_d D_{\text{eff}} \quad (4.11)$$

where the effective diffusion coefficient D_{eff} is,

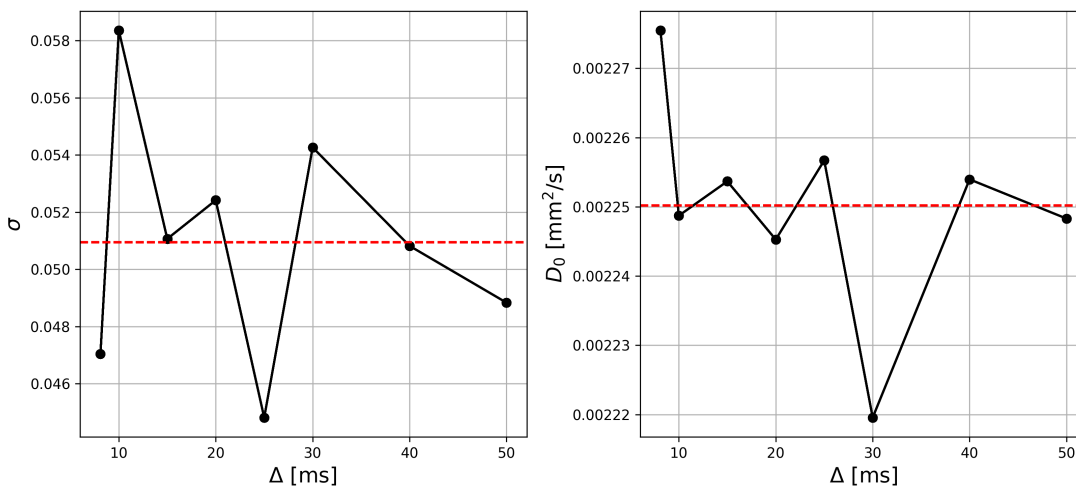
$$D_{\text{eff}} = D_0 (1 + \sigma \sin^2 \theta) \quad (4.12)$$

Consequently, the new diffusion coefficient D_{eff} depends on both the angle and

the gradient correction.



(a)



(b)

Figure 4.4: (a) The plot illustrates the fit 4.12 applied to the corrected curves of the experimental values of the diffusion coefficient as a function of θ . (b) The fitting parameters σ and D_0 are displayed. A red horizontal line indicates the mean value of each parameter.

Recalling that the experimental curves in Figure 4.3 exhibited an increasing behavior as a function of θ , we can adjust the effective diffusion coefficient D_{eff} since it includes the term that accounts for this behavior due to the angle θ and σ , which contains information about the gradient. Therefore, by fitting the experimental curves using Equation (4.12), we can obtain the numerical values that model these parameters.

Thus, through data fitting (Figure 4.4a), we obtain:

$$\sigma = 5.10 \times 10^{-2} \quad (4.13)$$

and,

$$D_0 = 2.25 \times 10^{-3} \frac{\text{mm}^2}{\text{s}} \quad (4.14)$$

The value D_0 is which it is going to be used to normalize the fiber curves. It is also the value referred to as the unrestricted diffusion coefficient.

4.2 Geometrical Analysis of Restricted Diffusion

4.2.1 Restricted Diffusion as a Function of Diffusion Time

Δ

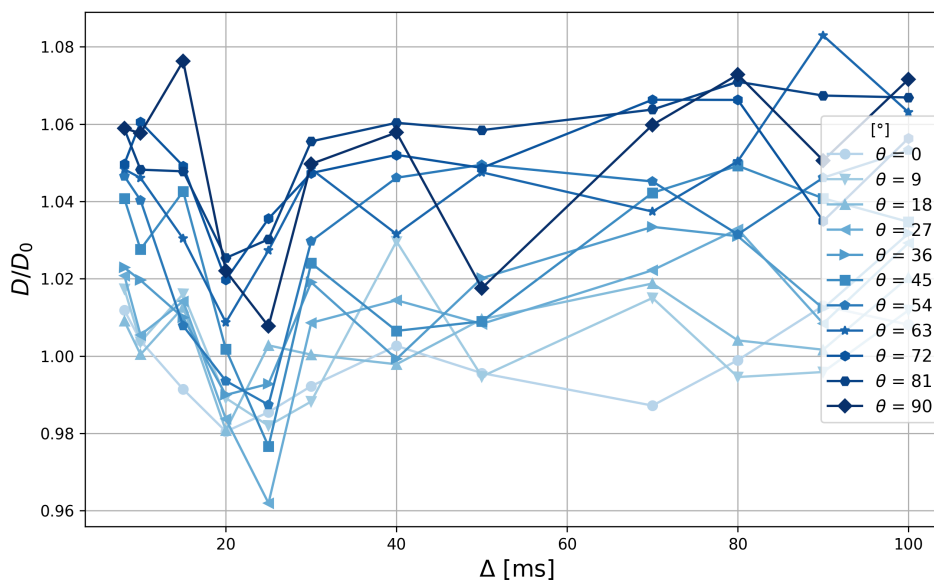


Figure 4.5: Corrected free water normalized diffusion coefficient as a function of Δ

Given that the corrected plot of the free water diffusion coefficient as a function of diffusion time display a constant behavior—characterized by noise, which manifests not as systematic but as consistent fluctuations—this outcome aligns with theoretical expectations, see Figure 4.5. It demonstrates that the diffusion coefficient remains unchanged with an increase in diffusion time for free water. This constancy underscores that the expression for D_{eff} is correctly formulated to depend solely on the gradient orientation.

Since no additional correction is needed for D_{eff} in relation to Δ in an unrestricted medium, the next step is to adjust the fiber data using the D_{eff} correction to calculate D_{app} . This corrected value depends on both the gradient orientation θ and the diffusion time Δ for the restricted medium.

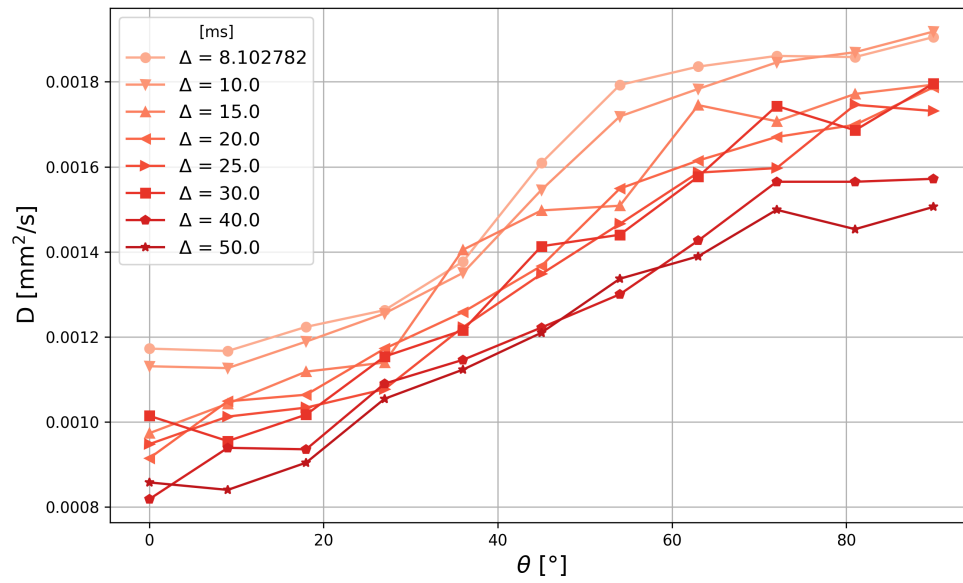
4.2.2 Restricted Diffusion as a Function of Diffusion Orientation θ

The diffusion coefficient is influenced by factors such as gradient intensity, diffusion time, and surface restrictions. Consequently, the new diffusion coefficient, D_{app} , is defined as:

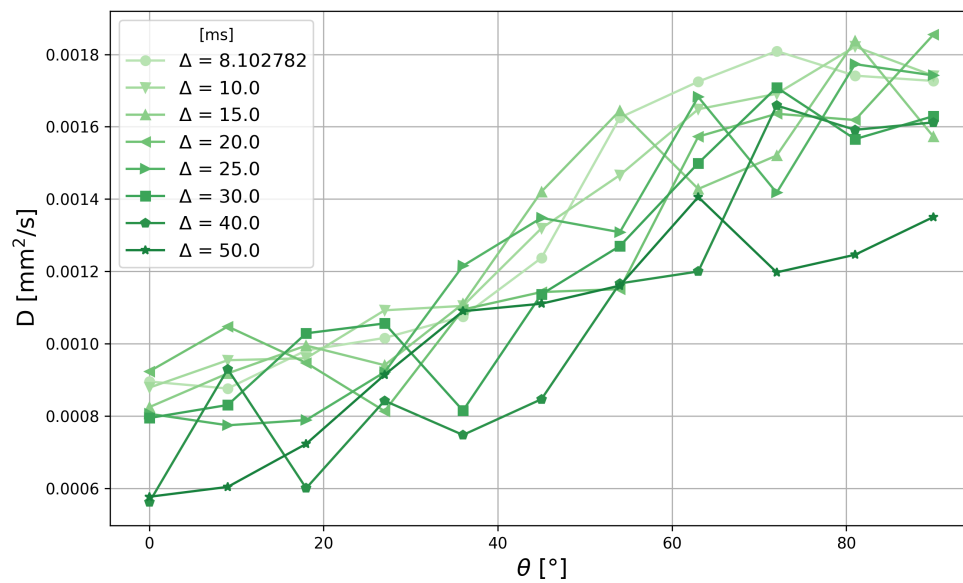
$$D_{\text{app}} = \frac{D}{1 + \sigma \sin^2 \theta} \quad (4.15)$$

Here, D represents the experimental values obtained initially, and σ is the parameter determined for the unrestricted correction (4.13).

Given the porous media behavior of both the large and small fibers, they will exhibit restricted medium characteristics. This behavior depends on both θ and Δ , resulting in the following corrected curves:

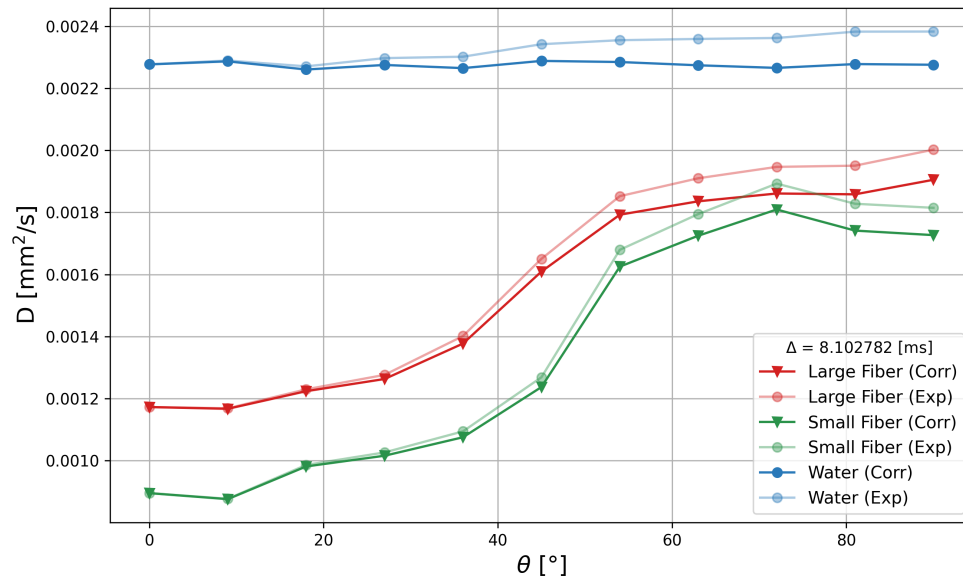


(a)

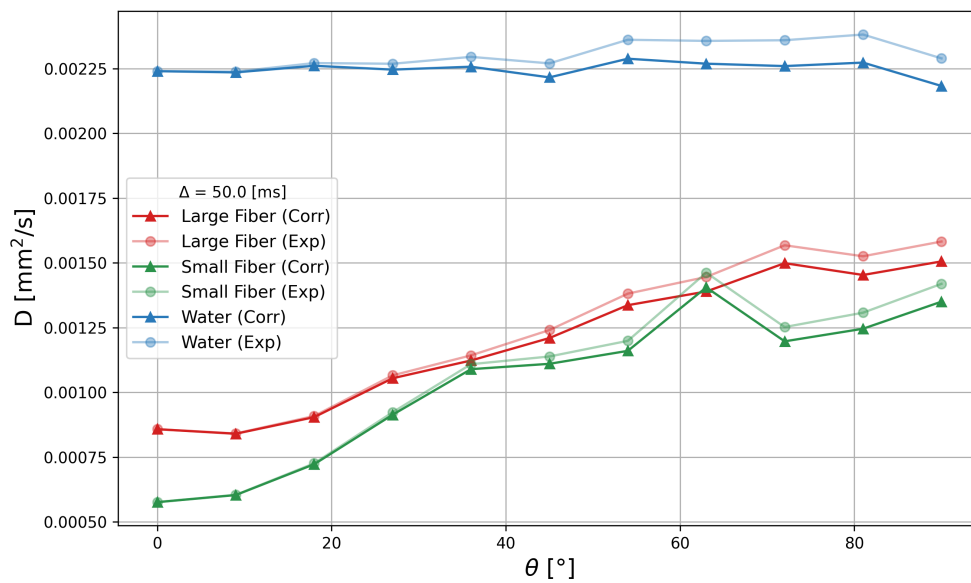


(b)

Figure 4.6: (a) and (b) depict the D versus θ plots for large and small fibers, respectively. In both graphs, the curves represent the corrected apparent diffusion coefficient (D_{app}) values.



(a)



(b)

Figure 4.7: (a) and (b) depict the D versus θ plots for large fiber, small fiber, and free water at diffusion times $\Delta = 8.102782$ ms and $\Delta = 50.0$ ms, respectively. The blue curves represent free water, red curves represent large fibers, and green curves represent small fibers. Both experimental (Exp) and corrected (Corr) data are shown.

The Figures 4.7 illustrate the behavior of the diffusion coefficient D as a function of the angle θ for different diffusion times. For free water (blue curves), the corrected data maintains a constant behavior across θ , indicating consistent diffusion properties as expected.

In the case of the fibers, the corrected curves do not flatten completely because the diffusion coefficient is expected to increase with the angle θ . This increase is due to a reduced collision frequency with restrictions, such as walls, at higher angles. While the corrected fiber curves initially match the experimental data, they diverge as θ increases due to the applied gradient correction.

Specifically, Figure 4.7a shows smoother curves compared to Figure 4.7b, which displays some noise attributed to the longer diffusion time. The smoothing effect in the shorter diffusion time plot is indicative of less complex interactions within the medium, whereas the noise in the longer diffusion time plot suggests increased complexity and potential artifacts. These observations are critical for validating the correction applied to the diffusion measurements and understanding the underlying physical processes in different media.

4.2.3 Fibers Diffusion as a Function of Diffusion Time Δ

For *short diffusion times*, the motion of diffusing particles is primarily governed by their free path before encountering any barriers. In this regime, the diffusion coefficient can be approximated by considering the immediate interactions of particles with the pore boundaries. This behavior is characterized by a time-dependent

relationship, often described by a term involving $\sqrt{D_0 t}$ [11]. The short-time approximation is crucial for understanding how particles initially interact with the microstructure of the medium, giving insight into the surface-area-to-volume ratio (S/V_p) and the initial boundary effects on diffusion [12].

In the *intermediate time regime*, particles begin to encounter the geometric constraints of the medium more frequently. This results in a more complex time dependence of the diffusion coefficient, which can be captured by terms like β/t . The intermediate regime reflects the transition from free diffusion to the restricted diffusion imposed by the microstructure of the medium [13]. During this period, the diffusion process is influenced by the size and connectivity of the pores, as well as the overall arrangement of obstacles within the medium.

For *long diffusion times*, the effective diffusion coefficient approaches a steady state, reflecting the overall connectivity and structural complexity of the medium. The long-time behavior is often dominated by the tortuosity of the medium explained in Section 3.1.3. The steady-state value provides insight into the extent to which the medium impedes diffusion relative to free diffusion. At this stage, the diffusion process is significantly influenced by the tortuosity, which quantifies how convoluted the path of the diffusing particles is due to the medium's structure.

The subsequent step involves analyzing the behavior of the corrected curves depicted in Figure 4.6 and interpreting their implications with respect to time and size. To accomplish this, two phenomenological models will be used: the Power Law and the Padé Approximant. These models will facilitate the derivation of results based on the parameters adjusted for our curves. In this part of the fitting

of D/D_0 vs Δ , only the large fiber ROI will be used because the plot of the small fiber is very noisy and contains many artifacts, making it difficult to adjust the data to the phenomenological models.

Power Law Model

The Power Law model:

$$\frac{D(t)}{D_0} = \frac{1}{\alpha} + \frac{\beta_1}{t} - \frac{\beta_2}{t^{3/2}} \quad (4.16)$$

is particularly useful for describing the diffusion process over a wide range of timescales [14]. This model captures the initial, intermediate, and long-term behaviors of diffusion in a porous medium through its parameters. The parameter α represents the long-time steady-state diffusion behavior, indicating the tortuosity of the medium. A higher α value suggests greater impediments to diffusion due to a more tortuous path. The term β_1/t describes the intermediate time regime, where particles frequently encounter geometric constraints, providing insight into the pore size and the connectivity of the medium. Additionally, $\beta_2/t^{3/2}$ accounts for the complex long-term interactions and hindrances, reflecting the overall structural complexity of the medium.

The Power Law model is ideal for scenarios requiring a detailed understanding of the diffusion process across multiple timescales, especially when dealing with media that have complex structures with varying tortuosity and connectivity. In our analysis, the parameter β_2 was set to zero. This decision was based on data adjustments showing that β_2 was sufficiently close to zero, justifying its exclusion

from the model. As a result:

$$\frac{D(t)}{D_0} = \frac{1}{\alpha} + \frac{\beta_1}{t} \quad (4.17)$$

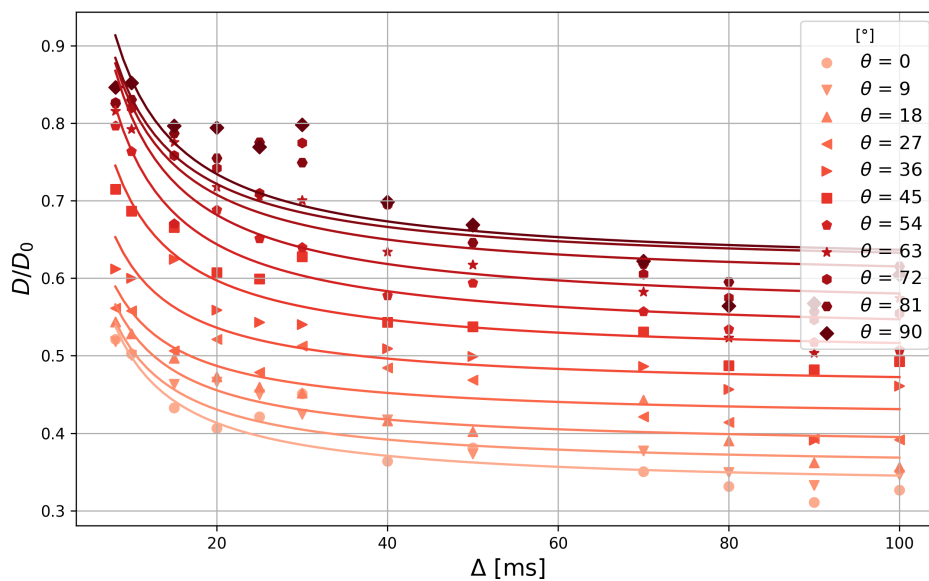


Figure 4.8: Experimental data of Large fiberfibers D/D_0 as a function of Δ fitted with the Power Law model. The scatter points represent the experimental data, while the curves represent the fitting.

Padé Approximant

The Padé approximant offers a robust method for interpolating between the short-time and long-time diffusion behaviors. It is expressed as follows:

$$\frac{D(t)}{D_0} = 1 - \left(1 - \frac{1}{\alpha}\right) \frac{c\sqrt{t} + (1 - 1/\alpha)t/\Theta}{(1 - 1/\alpha) + c\sqrt{t} + (1 - 1/\alpha)t/\Theta} \quad (4.18)$$

The parameters in this model are designed to capture different aspects of the diffusion process. The term $(1 - 1/\alpha)$ represents the deviation from the steady-state diffusion behavior due to tortuosity. The parameter $c\sqrt{t}$ captures the short-time diffusion behavior, reflecting the initial interactions of diffusing particles with the pore walls. Here, $c = (4/9\sqrt{\pi})(S/V_p)(D_0)$, where S/V_p is the surface-area-to-volume ratio of the pores [1]. Additionally, $(1 - 1/\alpha)t/\Theta$ accounts for the intermediate and long-time diffusion behaviors, providing a smooth transition between the short-time and long-time limits. Θ is a fitting parameter with dimensions of time, scaling with the square of the pore size.

It will be set c to zero because the experimental setup does not achieve the microtime and microstructure resolution required to observe short-time diffusion effects. This simplification is appropriate as it eliminates the short-time term from the Padé approximant, focusing the analysis on the intermediate and long-time diffusion behaviors, which are more relevant to our study. By setting c to zero, the equation simplifies to:

$$\frac{D(t)}{D_0} = 1 - \left(1 - \frac{1}{\alpha}\right) \frac{t/\Theta}{1 + t/\Theta} \quad (4.19)$$

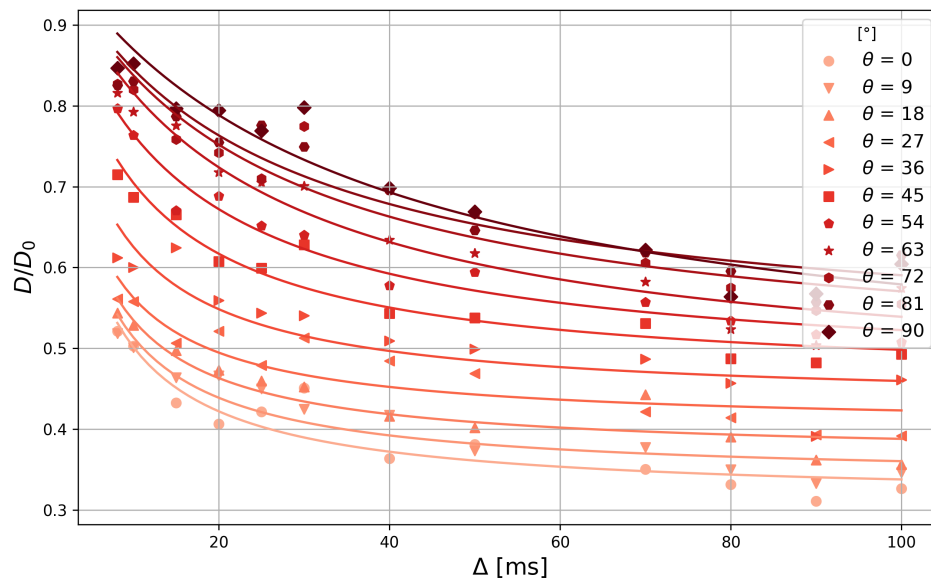


Figure 4.9: Experimental data of fibers D/D_0 as a function of Δ fitted with the Padé Approximant. The scatter points represent the experimental data, while the curves represent the fitting.

This adjustment focuses our analysis on the more significant intermediate and long-term effects, providing a clearer understanding of how tortuosity and the medium's structure influence diffusion over these timescales.

Chapter 5

Quantitative analysis of the hindered diffusion within the extra-axonal space

5.1 Diffusion Parameters

5.1.1 Tortuosity

Figure 5.1 illustrates the parameter $1/\alpha$ as a function of θ for both the Power Law and Padé Approximant models. Here, $1/\alpha$ represents the tortuosity of the medium, where higher values indicate more convoluted pathways. Both models show $1/\alpha$ increasing with θ , but the Power Law model consistently predicts higher

tortuosity. This suggests that the Power Law model might be more sensitive to changes in tortuosity or might overestimate the tortuosity compared to the Padé Approximant.

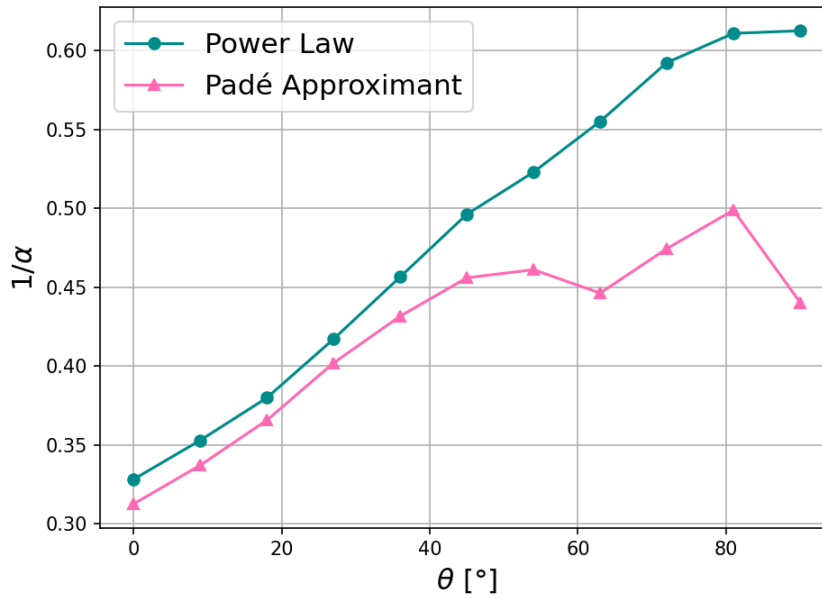


Figure 5.1: Tortuosity $1/\alpha$ as a function of θ for the Power Law and Padé Approximant models.

Notably, the Padé Approximant model shows $1/\alpha$ stabilizing at higher angles, indicating that the tortuosity reaches a constant value. This saturation suggests that beyond a certain angle, the medium's geometric constraints and diffusion paths have reached maximum complexity, and further increases in θ do not significantly affect the diffusion process. This saturation is crucial for our study as it indicates a limit to the tortuosity, reflecting a threshold in the medium's structural complexity.

Considering the cylindrical symmetry of the fibers, which are aligned along the z -axis, the angle $\theta = 0^\circ$ represents transverse diffusion. In this orientation, the diffusion path encounters the maximum number of obstacles due to the perpendicular arrangement of fibers, resulting in higher tortuosity. Conversely, at $\theta = 90^\circ$, the diffusion is parallel to the fibers, resembling more free diffusion with fewer obstructions, also explained in Figure 4.7. This geometrical setup explains why the tortuosity is lower at higher angles and why the Padé Approximant model shows saturation.

The angle at which this occurs signifies the point where the diffusion pathways are most intricately entangled transversely. Beyond this angle, further increases in θ align the diffusion paths more parallel to the fibers, thereby reducing the influence of structural constraints. Understanding this behavior provides insights into the geometrical and diffusive constraints within the medium, highlighting the importance of θ in determining the diffusion characteristics and the effective tortuosity of the system.

By analyzing the convergence behavior of $1/\alpha$ with θ , valuable information about the interaction between diffusion pathways and fiber alignment is obtained. The distinction between the models suggests that while both can describe the general trend, the Padé Approximant's saturation feature offers a more realistic depiction of the upper limits of tortuosity in highly structured media.

5.1.2 Convergence times to tortuosity

β_1 represents the characteristic timescale for the intermediate diffusion regime, capturing how quickly particles transition from free diffusion to encountering geometric constraints. This timescale is influenced by the microstructural barriers and the alignment of fibers.

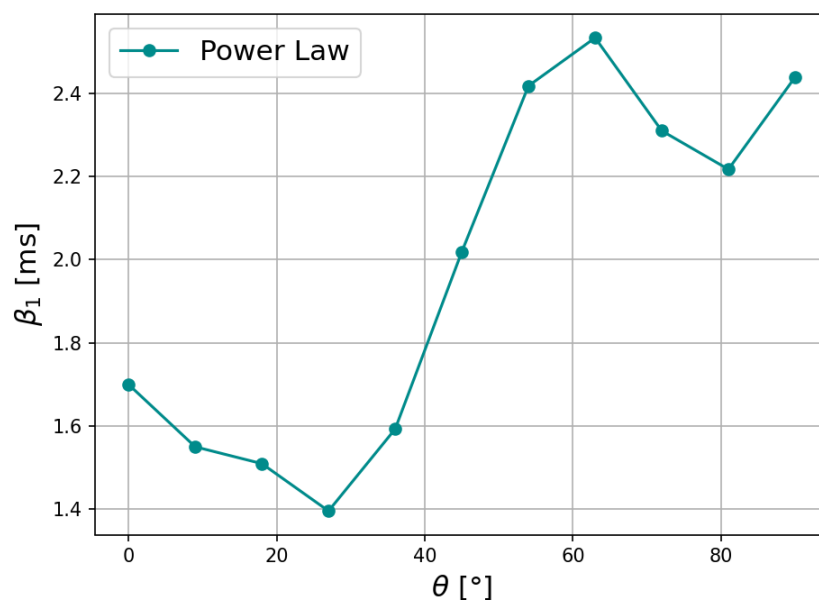


Figure 5.2: β_1 as a function of θ for the Power Law model.

The initial decrease in β_1 as θ increases suggests that up to $\theta \approx 40^\circ$, particles face more resistance in their diffusion pathways. This indicates that the fibers are aligned in a way that presents more obstructions to particle movement, making the diffusion process more tortuous and requiring a longer time for particles to transition from free diffusion to encountering significant geometric constraints.

Around $\theta = 40^\circ$, β_1 reaches a minimum, reflecting the most obstructed diffusion pathway with the highest resistance. Beyond this angle, β_1 increases, indicating that the diffusion paths become less obstructed and less tortuous, allowing for a quicker transition to the intermediate diffusion regime. This change in β_1 reflects the enhanced impact of microstructural barriers on the diffusion process, making the intermediate diffusion regime more significant.

In terms of the fiber geometry, at smaller angles, the particles move transversely to the fiber alignment, encountering more obstacles and a higher degree of tortuosity, which is why β_1 is lower. As θ increases towards 90° , the diffusion path aligns more optimally with the fiber structure, encountering fewer barriers and more resembling free diffusion, resulting in a higher β_1 . Thus, β_1 serves as an indicator of how the diffusion pathways change with the angle θ , highlighting the transitions between different diffusion regimes and the corresponding impact of microstructural barriers on the diffusion process.

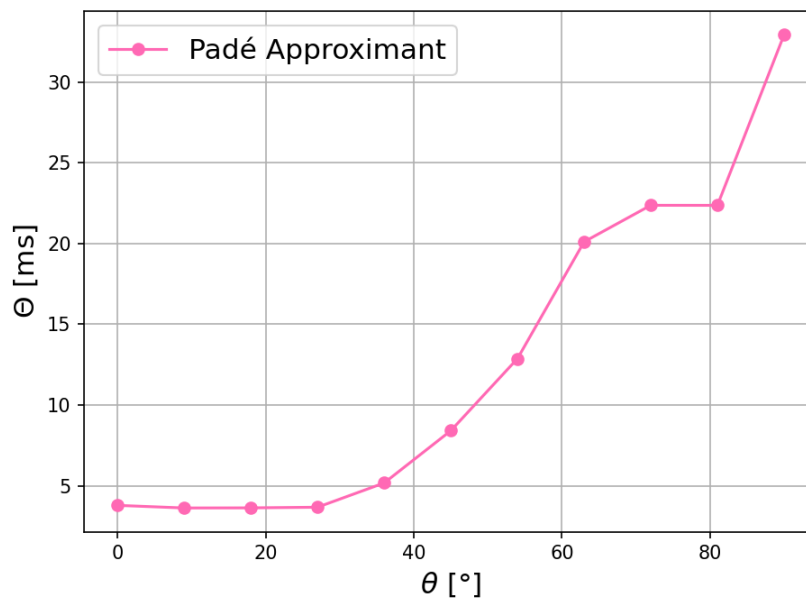


Figure 5.3: Θ as a function of θ for the Padé Approximant model.

Finally, Figure 5.3 presents Θ as a function of θ for the Padé Approximant model. Θ is a fitting parameter representing a characteristic time scale that influences the transition from short to long-time diffusion behavior. The plot shows that Θ increases with θ , remaining relatively low and stable for $\theta < 30^\circ$ and then increasing significantly.

For smaller angles, the time scale Θ is short, indicating that the transition from short to long-time behavior happens quickly due to the high number of obstacles encountered in the transverse direction. As θ increases, the diffusion path aligns more with the fibers, reducing the number of obstacles, which results in a longer transition time to the steady-state diffusion regime.

The significant increase in Θ at higher angles reflects reduced geometric constraints and a shift towards free diffusion behavior. This indicates that the medium's complexity and connectivity impact the diffusion dynamics, with longer Θ values at higher angles suggesting that diffusion in these directions remains less restricted for longer periods before transitioning to the steady-state behavior.

In the Padé Approximant model, the term t/Θ decreases as Θ increases, showing that higher Θ values lead to a slower transition from short to long-time diffusion behavior. This is consistent with the physical interpretation that at higher angles, the particles experience fewer geometric constraints, and the diffusion remains in the short-time regime for an extended period.

Chapter 6

Conclusions

The initial phase of the study focused on identifying and correcting artifacts that could potentially distort the diffusion measurements. By calibrating the gradient system and accounting for errors related to gradient orientation, induced by hardware calibration errors, we ensured the reliability of the experimental data. The calibration process revealed a dependency of the gradient on the angle θ , leading to the formulation of an effective diffusion coefficient D_{eff} that considers these variations. This correction was encapsulated in the parameter D_{app} , which includes the factor σ to account for gradient inconsistencies. Notably, the measured diffusion coefficient D_0 for the free diffusion of water was found to be $2.25 \times 10^{-3} \text{ mm}^2/\text{s}$, consistent with the literature value for water at $T = 25^\circ\text{C}$ [15].

The study employed two primary models to characterize the diffusion parameters: the Power Law model and the Padé Approximant. These models provided insights into the diffusion behavior across different time scales, capturing the nu-

ances of short-term, intermediate, and long-term diffusion processes. The Power Law model was particularly useful for describing the steady-state diffusion behavior and the intermediate regime, while the Padé Approximant offered a robust method for interpolating between different diffusion behaviors.

One of the objectives of this work was to characterize the diffusion of the phantom assembled in the laboratory in different spatial directions. This complements previous characterizations conducted in the laboratory, which were limited to a single spatial direction. This objective was successfully achieved through data analysis.

The results demonstrated that tortuosity, a measure of the complexity of diffusion pathways, varied significantly with the angle of diffusion orientation. The Padé Approximant model revealed that tortuosity approaches a constant value at higher angles, indicating a saturation point beyond which additional increases in θ do not significantly affect the diffusion process. This finding underscores the importance of geometric constraints in influencing diffusion dynamics.

The study identified characteristic timescales for the transition from free diffusion to restricted diffusion, influenced by the alignment of fibers and the structural complexity of the medium. The parameter β_1 , representing the intermediate diffusion regime, showed a minimum at $\theta \approx 40^\circ$, reflecting the most obstructed diffusion pathway. This transition is crucial for understanding how particles interact with microstructural barriers over time.

This study contributes to the field of NMR and diffusion research by offering

a refined approach to measuring and characterizing diffusion in structured media. The integration of artifact correction and advanced modeling techniques enhances the accuracy of diffusion measurements, providing deeper insights into the underlying physical processes.

The next step in this research is to apply the equations for correlation length and correlation time to the corrected diffusion curves obtained in this study. These equations will require numerical solutions to fully capture the dynamics of diffusion in porous media. The correlation length reflects the average distance over which particles are affected by the microstructure, while the correlation time represents the timescale over which particles experience these structural influences. Understanding these parameters will provide deeper insights into the physical behavior of diffusion in complex media, enabling more precise modeling and prediction of diffusion processes.

Future research should focus on further refining the models used in this study and exploring their applicability to other types of structured media. Additionally, the development of more sophisticated calibration techniques and the incorporation of higher-resolution imaging methods could provide even greater insights into diffusion processes at the microscopic level.

In conclusion, this study successfully addressed the challenges of artifact correction and diffusion parameter characterization in NMR, offering valuable contributions to the understanding of molecular diffusion in porous media. The findings underscore the importance of precise calibration and advanced modeling in achieving accurate and meaningful results in diffusion research.

Furthermore, the methodologies and findings of this study have significant implications for clinical applications. By enhancing our ability to accurately measure and characterize diffusion in structured media, we can improve imaging techniques used in medical diagnostics, such as axonal imaging for early detection of neurological conditions. This approach can also aid in the characterization of different tissues and pathological pathways, leading to better diagnosis and treatment planning in various medical fields. The ability to precisely model diffusion in complex biological tissues could revolutionize our understanding and management of diseases, ultimately contributing to more effective and personalized healthcare solutions.

Bibliography

- [1] Paul T Callaghan. *Translational dynamics and magnetic resonance: principles of pulsed gradient spin echo NMR*. Oxford University Press, 2011.
- [2] Nadine Barrie Smith and Andrew Webb. *Introduction to medical imaging: physics, engineering and clinical applications*. Cambridge university press, 2010.
- [3] H Lassmann. Axonal injury in multiple sclerosis, 2003.
- [4] Gorazd B Stokin and Lawrence SB Goldstein. Axonal transport and alzheimer's disease. *Annu. Rev. Biochem.*, 75:607–627, 2006.
- [5] Denis Le Bihan and Eric Breton. Imagerie de diffusion in-vivo par résonance magnétique nucléaire. *Comptes-Rendus de l'Académie des Sciences*, 93(5):27–34, 1985.
- [6] Clifford R Jack, David S Knopman, William J Jagust, Leslie M Shaw, Paul S Aisen, Michael W Weiner, Ronald C Petersen, and John Q Trojanowski. Hypothetical model of dynamic biomarkers of the alzheimer's pathological cascade. *The Lancet Neurology*, 9(1):119–128, 2010.

- [7] Robert W Brown, Y-C Norman Cheng, E Mark Haacke, Michael R Thompson, and Ramesh Venkatesan. *Magnetic resonance imaging: physical principles and sequence design*. John Wiley & Sons, 2014.
- [8] Anatole Abragam. *The principles of nuclear magnetism*. Number 32. Oxford university press, 1961.
- [9] Edward O Stejskal and John E Tanner. Spin diffusion measurements: spin echoes in the presence of a time-dependent field gradient. *The journal of chemical physics*, 42(1):288–292, 1965.
- [10] Ezequiel L. Saidman. Filtros selectivos de dinámicas traslacionales en microestructuras de materia blanca con mri. Master’s thesis, Instituto Balseiro, Universidad Nacional de Cuyo, Comisión Nacional de Energía Atómica, Argentina, December 2022. Supervised by Dr. Gonzalo A. Álvarez.
- [11] Lawrence L Latour, Partha P Mitra, Robert L Kleinberg, and Christopher H Sotak. Time-dependent diffusion coefficient of fluids in porous media as a probe of surface-to-volume ratio. *Journal of Magnetic Resonance, Series A*, 101(3):342–346, 1993.
- [12] Ross W Mair, Pabitra N Sen, Martin D Hürlimann, Samuel Patz, David G Cory, and Ronald L Walsworth. The narrow pulse approximation and long length scale determination in xenon gas diffusion nmr studies of model porous media. *Journal of Magnetic Resonance*, 156(2):202–212, 2002.
- [13] Paul Heitjans and Jörg Kärger. *Diffusion in condensed matter: methods, materials, models*. Springer Science & Business Media, 2006.

- [14] Thomas M de Swiet and Pabitra N Sen. Time dependent diffusion coefficient in a disordered medium. *The Journal of chemical physics*, 104(1):206–209, 1996.
- [15] Allan J Easteal, William E Price, and Lawrence A Woolf. Diaphragm cell for high-temperature diffusion measurements. tracer diffusion coefficients for water to 363 k. *Journal of the Chemical Society, Faraday Transactions 1: Physical Chemistry in Condensed Phases*, 85(5):1091–1097, 1989.